



UPPSALA  
UNIVERSITET

*Digital Comprehensive Summaries of Uppsala Dissertations  
from the Faculty of Science and Technology 772*

# Insights into Materials Properties from Ab Initio Theory

*Diffusion, Adsorption, Catalysis & Structure*

ANDREAS BLOMQVIST



ACTA  
UNIVERSITATIS  
UPSALIENSIS  
UPPSALA  
2010

ISSN 1651-6214  
ISBN 978-91-554-7907-7  
urn:nbn:se:uu:diva-131331



Dissertation presented at Uppsala University to be publicly examined in Siegbansalen, Ångströmlaboratoriet, Lägerhyddsvägen 1, Uppsala, Friday, November 12, 2010 at 10:15 for the degree of Doctor of Philosophy. The examination will be conducted in English.

#### Abstract

Blomqvist, A. 2010. Insights into Materials Properties from Ab Initio Theory. *Diffusion, Adsorption, Catalysis & Structure*. Acta Universitatis Upsaliensis. *Digital Comprehensive Summaries of Uppsala Dissertations from the Faculty of Science and Technology* 772. 81 pp. Uppsala. ISBN 978-91-554-7907-7.

In this thesis, density functional theory (DFT) calculations and DFT based *ab initio* molecular dynamics simulations have been employed in order to gain insights into materials properties like diffusion, adsorption, catalysis, and structure.

In transition metals, absorbed hydrogen atoms self-trap due to localization of metal d-electrons. The self-trapping state is shown to highly influence hydrogen diffusion in the classical over-barrier jump temperature region. Li diffusion in Li-N-H systems is investigated. The diffusion in  $\text{Li}_3\text{N}$  is shown to be controlled by the concentration of vacancies. Exchanging one Li for H ( $\text{Li}_2\text{NH}$ ), gives a system where the diffusion no longer is dependent on the concentrations of vacancies, but instead on N-H rotations. Furthermore, exchanging another Li for H ( $\text{LiNH}_2$ ), results in a blockade of Li diffusion. For high-surface area hydrogen storage materials, metal organic frameworks and covalent organic frameworks, the hydrogen adsorption is studied. In metal organic frameworks, a Li-decoration is also suggested as a way to increase the hydrogen adsorption energy. In  $\text{NaAlH}_4$  doped with transition metals (*TM*), the hypothesis of *TM*-Al intermetallic alloys as the main catalytic species is supported. The source of the catalytic effect of carbon nanostructures on hydrogen desorption from  $\text{NaAlH}_4$  is shown to be the high electronegativity of the carbon nanostructures. A space-group optimized *ab initio* random structure search method is used to find a new ground state structure for  $\text{BeC}_2$  and  $\text{MgC}_2$ . The fast change between the amorphous and the crystalline phase of GeSbTe phase-change materials is suggested to be due to the close resemblance between the local amorphous structure and the crystalline structure. Finally, we show that more than 80% of the voltage in the lead acid battery is due to relativistic effects.

**Keywords:** Density functional theory, Molecular dynamics, Diffusion, Catalysis, Adsorption, Random structure search, Hydrogen-storage materials, Phase-change materials

Andreas Blomqvist, Department of Physics and Astronomy, Materials Theory, Box 516, Uppsala University, SE-751 20 Uppsala, Sweden.

© Andreas Blomqvist 2010

ISSN 1651-6214

ISBN 978-91-554-7907-7

urn:nbn:se:uu:diva-131331 (<http://urn.kb.se/resolve?urn=urn:nbn:se:uu:diva-131331>)

*To Moa*

# List of Papers

This thesis is based on the following papers, which are referred to in the text by their Roman numerals.

- I    **The significance of self—trapping on hydrogen diffusion**  
Andreas Blomqvist, Gunnar K. Pálsson, C. Moyses Araujo, Rajeev Ahuja, and Björgvin Hjörvarsson  
*Physical Review Letters*, In Press (2010)
  
- II   **Superionicity in the hydrogen storage material  $\text{Li}_2\text{NH}$ : Molecular dynamics simulations**  
C. Moyses Araujo, Andreas Blomqvist, Ralph H. Scheicher, Ping Chen, and Rajeev Ahuja  
*Physical Review B* **79**, 172101 (2009)
  
- III   **Hydrogen as Promotor and Inhibitor of Superionicity in the Li–N–H Systems**  
Andreas Blomqvist, C. Moyses Araujo, Ralph H. Scheicher, Pornjuk Srepusharawoot, Wen Li, Ping Chen, and Rajeev Ahuja  
*Physical Review B* **82**, 024304 (2010)
  
- IV    **$\text{Li}^+$  Ion Conductivity and Diffusion Mechanism in  $\alpha\text{-Li}_3\text{N}$  and  $\beta\text{-Li}_3\text{N}$**   
Wen Li, Guotao Wu, C. Moyses Araujo, Ralph H. Scheicher, Andreas Blomqvist, Rajeev Ahuja, Zhitao Xiong, Yuanping Feng and Ping Chen  
*Energy & Environmental Science* **3**, 1524(2010)
  
- V    **Li–decorated metal–organic framework 5: A route to a suitable hydrogen storage material**  
A. Blomqvist, C. Moyses Araujo, P. Srepusharawoot, and R. Ahuja  
*Proceedings of the National Academy of Science of the U.S.A.* **104**, 20173 (2007)
  
- VI   **A comparative investigation of  $\text{H}_2$  adsorption strength in Cd– and Zn–based metal organic framework–5**  
Pornjuk Srepusharawoot, C. Moyses Araujo, Andreas Blomqvist, Ralph H. Scheicher, and Rajeev Ahuja  
*Journal of Chemical Physics* **129**, 164104 (2008)

- VII **Hydrogen Binding in Alkali-decorated Iso-reticular Metal Organic Framework-16 based on Zn, Mg, and Ca**  
 Pornjuk Srepusharawoot, Andreas Blomqvist, Ralph H. Scheicher, C. Moyses Araujo, and Rajeev Ahuja  
*Submitted*
- VIII **Ab Initio Study of Molecular Hydrogen Adsorption in Covalent Organic Framework-1**  
 Pornjuk Srepusharawoot, Ralph H. Scheicher, C. Moyses Araujo, Andreas Blomqvist, Udomsilp Pinsook, and Rajeev Ahuja  
*Journal of Physical Chemistry C* **113**, 8498 (2009)
- IX **Dehydrogenation from 3d-transition-metal-doped NaAlH<sub>4</sub>: Prediction of catalysts**  
 Andreas Blomqvist, C. Moyses Araujo, Puru Jena, and Rajeev Ahuja  
*Applied Physics Letters* **90**, 149004 (2007)
- X **Ti-induced destabilization of NaBH<sub>4</sub> from first-principles theory**  
 C. Moyses Araujo, Andreas Blomqvist, and Rajeev Ahuja  
*Journal of Physics: Condensed Matter* **20**, 122202 (2008)
- XI **Carbon Nanomaterials as Catalysts for Hydrogen Uptake and Release in NaAlH<sub>4</sub>**  
 Polly A. Berseth, Andrew G. Harter, Ragaiy Zidan, Andreas Blomqvist, C. Moyses Araujo, Ralph H. Scheicher, Rajeev Ahuja, and Puru Jena  
*Nano Letters* **9**, 1501 (2009)
- XII **One-dimensional polymeric carbon structure based on five-membered rings in alkaline earth metal dicarbides BeC<sub>2</sub> and MgC<sub>2</sub>**  
 Pornjuk Srepusharawoot, Andreas Blomqvist, Ralph H. Scheicher, C. Moyses Araujo, and Rajeev Ahuja  
*Physical Review B* **82**, 024304 (2010)
- XIII **Substitutional alloy of Ce and Al**  
 Qiao-Shi Zeng, Yang Ding, Wendy L. Mao, Wei Luo, Andreas Blomqvist, Rajeev Ahuja, Wenge Yang, Jinfu Shu, Stas V. Sinogeikin, Yue Meng, Dale L. Brewe, Jian-Zhong Jiang, and Ho-kwang Mao  
*Proceedings of the National Academy of Science of the U.S.A.* **106**, 2515 (2009)

- XIV **Structural and energetic analysis of the hydrogen storage materials  $\text{LiNH}_2\text{BH}_3$  and  $\text{NaNH}_2\text{BH}_3$  from ab initio calculations**  
M. Ramzan, F. Silvearv, A. Blomqvist, R. H. Scheicher, S. Lebègue, and R. Ahuja  
*Physical Review B* **79**, 132102 (2009)
- XV **Local structure of liquid  $\text{Ge}_1\text{Sb}_2\text{Te}_4$  for rewritable data storage use**  
Z. Sun, J. Zhou, A. Blomqvist, L. Xu, and R. Ahuja  
*Journal of Physics: Condensed Matter* **20**, 205102 (2008)
- XVI **Fast crystallization of chalcogenide glass for rewritable memories**  
Zhimei Sun, Jian Zhou, Andreas Blomqvist, Börje Johansson, and Rajeev Ahuja  
*Applied Physics Letters* **93**, 061913 (2008)
- XVII **Stable nitride complex and molecular nitrogen in N doped amorphous  $\text{Ge}_2\text{Sb}_2\text{Te}_5$**   
Zhimei Sun, Jian Zhou, Hyun-Joon Shin, Andreas Blomqvist, and Rajeev Ahuja  
*Applied Physics Letters* **93**, 241908 (2008)
- XVIII **Formation of Large Voids in the Amorphous Phase-Change Memory  $\text{Ge}_2\text{Sb}_2\text{Te}_5$  Alloy**  
Zhimei Sun, Jian Zhou, Andreas Blomqvist, Börje Johansson, and Rajeev Ahuja  
*Physical Review Letters* **102**, 075504 (2009)
- XIX **First-principles investigation on the phase stability and chemical bonding of  $\text{mInSb-nInTe}$  phase-change random alloys**  
Naihua Miao, Baisheng Sa, Jian Zhou, Zhimei Sun, Andreas Blomqvist, Rajeev Ahuja  
*Solid State Communications* **150**, 1375 (2010)
- XX **Relativity and the lead-acid battery**  
Rajeev Ahuja, Andreas Blomqvist, Peter Larsson, Pekka Pyykkö, and Patryk Zaleski-Ejgierd  
*Submitted*

Reprints were made with permission from the publishers.

The following papers are co-authored by me, but not included in this thesis:

- **Potassium-Modified  $\text{Mg}(\text{NH}_2)_2/2 \text{ LiH}$  System for Hydrogen Storage**

J. Wang, T. Liu, G. Wu, W. Li, Y. Liu, C. M. Araujo, R. H. Scheicher, A. Blomqvist, R. Ahuja, Z. Xiong, P. Yang, M. Gao, H. Pan, and P. Chen

*Angewandte Chemie International Edition* **48**, 5828 (2009)

- **Understanding from First Principles why  $\text{LiNH}_2\text{BH}_3 \cdot \text{NH}_3\text{BH}_3$  Shows Improved Dehydrogenation over  $\text{LiNH}_2\text{BH}_3$  and  $\text{NH}_3\text{BH}_3$**

W. Li, R. H. Scheicher, C. M. Araujo, G. Wu, A. Blomqvist, C. Wu, R. Ahuja, Y. P. Feng and P. Chen

*Journal of Physical Chemistry*, In Press (2010)

Table 1: *The way I have contributed to the papers is indicated.*

Paper	designing research	performing calculations	analyzing data	developing analysis tools	writing the paper
I	•	•	•	•	•
II	•	•	•	•	•
III	•	•	•	•	•
IV			•		•
V	•	•	•	•	•
VI	•		•		•
VII	•	•	•		•
VIII	•		•		•
IX	•	•	•	•	•
X	•	•	•	•	•
XI	•	•	•	•	•
XII	•	•	•	•	•
XIII	•	•	•		•
XIV	•	•	•		•
XV			•	•	•
XVI			•	•	•
XVII			•	•	•
XVIII			•	•	•
XIX			•	•	•
XX		•	•		•

# Contents

1	Introduction	1
2	Density functional theory	3
2.1	The many body problem	3
2.2	Born–Oppenheimer approximation	3
2.3	Hohenberg–Kohn theorems	4
2.4	Kohn–Sham ansatz	5
2.5	Exchange–correlation functionals	6
2.6	Bloch electrons	6
2.7	Projector augmented–wave method	7
2.8	Force theorem	8
3	<i>Ab initio</i> molecular dynamics	9
3.1	Born–Oppenheimer molecular dynamics	9
3.2	Equilibration	10
3.3	Radial distribution function	10
3.4	Mean square displacement	11
3.5	Residence time	12
3.6	Bond angle distribution	12
3.7	Bond orientation distribution	13
3.8	Vibrational spectral density	13
4	Diffusion	15
4.1	Diffusion mechanism	15
4.2	Classical jump diffusion	15
4.2.1	Transition state theory or molecular dynamics	16
4.2.2	Harmonic transition state theory	16
4.3	Hydrogen diffusion in transition metals	17
4.3.1	Effects of self–trapping on diffusion in Nb	17
4.4	Lithium diffusion	23
4.4.1	Li diffusion in Li–N–H systems	23
4.4.2	Vibrational spectra of Li–N–H systems	26
4.4.3	Diffusion barriers in Li <sub>3</sub> N, $\alpha$ and $\beta$ phase	27
5	Adsorption	31
5.1	Strengthening the H <sub>2</sub> adsorption in MOF–5	32
5.2	The effect of metal oxide cluster	34
5.3	Alkali decorated (Zn–/Mg–/Ca–)IRMOF–16	37
5.4	Hydrogen interaction with COF–1	39
6	Catalysts	43
6.1	Hydrogen sorption catalysts, transition metals	44

6.1.1	NaAlH <sub>4</sub> . . . . .	44
6.1.2	NaBH <sub>4</sub> . . . . .	46
6.2	Hydrogen sorption catalysts, carbon nanostructures . . . . .	48
7	Structure . . . . .	51
7.1	<i>Ab initio</i> random search . . . . .	51
7.1.1	AIRS for BeC <sub>2</sub> structure . . . . .	52
7.2	Alloy of incompatible elements . . . . .	52
7.3	Structure of Li/Na–NH <sub>2</sub> BH <sub>3</sub> . . . . .	54
7.4	Phase–change materials . . . . .	56
7.4.1	Local structure of liquid and amorphous Ge <sub>1</sub> Sb <sub>2</sub> Te <sub>4</sub> . . . . .	56
7.4.2	N–doping of Ge <sub>2</sub> Sb <sub>2</sub> Te <sub>5</sub> . . . . .	57
7.4.3	Clustering of vacancies in Ge <sub>2</sub> Sb <sub>2</sub> Te <sub>5</sub> . . . . .	58
7.4.4	Phase stability of <i>m</i> InSb· <i>n</i> InTe . . . . .	59
7.5	Cars start due to relativity . . . . .	60
8	Conclusions and Outlook . . . . .	63
9	Acknowledgement . . . . .	65
10	Summary in Swedish . . . . .	67
	Table of Acronyms . . . . .	71
	Bibliography . . . . .	73

# 1. Introduction

*It is important to realize that in physics today, we have no knowledge of what energy is.*

— Richard Feynman

THROUGHOUT HISTORY, the progress of mankind has been closely connected to the materials used during that period, *e.g.* stone age, bronze age, and iron age. Today we are not only *discovering* new materials, but also actively *developing* them. This requires increasingly detailed understanding of the behaviour of matter. One of the tools in increasing our understanding, is large computers to carry out quantum mechanical calculations and simulations. In this thesis *ab initio* calculations as well as *ab initio* molecular dynamics simulations has been employed to that end.

An area with many challenging problems is hydrogen storage materials. The demand for energy is increasing all over the world. Simultaneously, the reserve of fossil fuels are shrinking and the effect of greenhouse gases is being considered a growing threat to our environment. For these reasons, the search for new technologies capable of replacing the fossil fuels has started. The use of hydrogen as a synthetic fuel, known as the hydrogen economy [1–3], is a potential candidate due to the following reasons: hydrogen has the highest energy per mass ratio of all chemical fuels, hydrogen is an abundant element on earth, and hydrogen can be burned in a combustion engine or electrochemically used in a fuel cell producing energy with only water as byproduct. One of the key issues to make this technology possible, is to find a hydrogen storage material with good storage properties [2–4].

A suitable hydrogen storage system for application in vehicles has to fulfil a number of criteria [2–5]. (i) The content of hydrogen (stored energy density) requires, high gravimetric hydrogen density (7.5 wt%) and high volumetric hydrogen density (70 kg H<sub>2</sub>m<sup>-3</sup>). This limits the elements that can be used in storage material to light-weight elements. (ii) Moreover, the storage material should be cost effective, safe, and non-toxic. (iii) The practical cycling properties of the hydrogen (un-)loading of the material furthermore requires, fast reversible sorption of hydrogen (kinetics) and a favourable working temperature (thermodynamics). In order to solve this problem, we need to find a material with the proper thermodynamic and kinetic properties.

A different area, data storage, requires increasingly higher storage densities. Mobile application require memories to be energy efficient. Phase-change materials can be used to store data in a non-volatile fashion, both in optical storage media, *e.g.* compact discs (CD) or digital versatile disks (DVD), and

in electric random access memory (RAM) [6]. Phase-change materials show distinct differences, both in optical and electrical properties, between the crystalline and the amorphous phase. The fast crystallization, a requirement to be used as a data storage material, is not yet fully understood. Understanding the mechanism behind the fast crystallization could help to find new materials with lower melting temperature, and hence, a lower energy requirement.

The two first chapters give a short overview of the background theory for density functional theory and *ab initio* molecular dynamics. The following four chapters contain results and discussions, divided into four different areas, namely, diffusion, adsorption, catalysis, and structure.

Diffusion, or the mass transport through a material, is one of the key properties for many materials today, *e.g.* battery materials, hydrogen storage materials, fuel cells, and smart windows are dependent on good diffusion properties. In Chapter 4, we explore the diffusion of hydrogen in transition metals and of lithium in Li–N–H systems.

The length scale of nano-structured materials present many new possibilities, *e.g.* the adsorption of molecules on the surface of high-surface area materials show promising results for application in hydrogen storage, separation of gases, and sensing applications. In Chapter 5, we investigate the adsorption of hydrogen molecules in porous framework materials. Furthermore, we propose a way to strengthen the interaction between the framework and the hydrogen gas.

In order to make chemical reactions efficient with respect to the energy and time requirement for a reaction, catalysts often play a key role. This is especially true in applications where you want to cycle a gas back and forth into a material, where you have a lot of bond reconstructions. In Chapter 6, we discuss the effect of transition metals and carbon nanostructures as catalyst for hydrogen sorption in  $\text{NaAlH}_4$  and  $\text{NaBH}_4$ .

In order to understand the basic properties of a material it is essential to know the structure of the material. Predicting the structure of a material, guided or unguided by experimental data, has been a long standing challenge in computational materials physics. In Chapter 7, we demonstrate a space group optimized random structure search method, which is used to find a new ground state structure for  $\text{BeC}_2$  and  $\text{MgC}_2$ . We also show how the incompatible elements, Ce and Al, can form a random alloy under pressure. Furthermore, we investigate the local structure of liquid and amorphous phase-change materials. Finally, we will show as an example of everyday relativity, that the cell voltage in lead-acid batteries arises from relativistic effects in the Pb-compounds.

## 2. Density functional theory

*The fundamental laws necessary for the mathematical treatment of a large part of physics and the whole of chemistry are thus completely known, and the difficulty lies only in the fact that application of these laws leads to equations that are too complex to be solved.*

— Paul Dirac

### 2.1 The many body problem

IN SOLID STATE PHYSICS, we are interested in understanding the way a number of atoms interact with each other, hence we are dealing with a many body problem. The properties of matter can be determined by solving the Schrödinger equation

$$\hat{H}\Psi = E\Psi. \quad (2.1)$$

The Hamiltonian,  $\hat{H}$ , can be split up,

$$\begin{aligned} \hat{H} = & -\frac{\hbar^2}{2} \sum_k^{N_{nuc}} \frac{\nabla^2}{M_k} - \frac{\hbar^2}{2} \sum_i^{N_{el}} \frac{\nabla^2}{m_e} \\ & + \frac{1}{2} \sum_{k \neq l}^{N_{nuc}} \frac{Z_k Z_l e^2}{|\mathbf{R}_k - \mathbf{R}_l|} + \frac{1}{2} \sum_{i \neq j}^{N_{el}} \frac{e^2}{|\mathbf{r}_i - \mathbf{r}_j|} - \sum_{i,k}^{N_{el}; N_{nuc}} \frac{Z_k e^2}{|\mathbf{r}_i - \mathbf{R}_k|}, \end{aligned} \quad (2.2)$$

where the first two terms are the kinetic energy operators of the nuclei and the electrons, and the last three terms are the interaction operators between nuclei–nuclei, electron–electron, and nuclei–electron.

However, the only system that can be solved exactly is the hydrogen atom, even for the helium atom we can not solve the problem exactly. In solids the problem becomes even worse since we are dealing with a large number of particles and consequently different levels of approximations have to be done.

### 2.2 Born–Oppenheimer approximation

The first approximation we will do is the Born–Oppenheimer approximation [7], which states that the motion of the electrons and the nuclei can be

considered separable. Since the mass of the nuclei is much larger than that of the electrons, the nuclei are considered frozen at their equilibrium positions. Meaning that when looking at the electrons, the nuclei can be considered stationary and the interaction between nuclei and electrons can be looked upon as an external potential,  $\hat{V}_{ext}$ , to the electrons. The interaction between nuclei is not of interest when describing the electrons and their contribution to the total energy of the system can be added later. After employing the Born–Oppenheimer approximation, the Hamiltonian of the electrons can now be written as

$$\hat{H}_e = -\frac{\hbar^2}{2} \sum_i^{N_{el}} \frac{\nabla^2}{m_e} + \frac{1}{2} \sum_{i \neq j}^{N_{el}} \frac{e^2}{|\mathbf{r}_i - \mathbf{r}_j|} + \hat{V}_{ext}. \quad (2.3)$$

In the external potential, external forces like the ones induced by electromagnetic fields can also be included. However, the electron–electron interaction is not trivial to solve. One approach, as we have used here, is to use density functional theory (DFT). In the next sections, we will give a brief background to DFT.

## 2.3 Hohenberg–Kohn theorems

Density functional theory is based on the Hohenberg–Kohn theorems [8].

**Theorem I:** For any system of interacting particles in an external potential  $V_{ext}(\mathbf{r})$ , the potential  $V_{ext}(\mathbf{r})$  is determined uniquely, except for a constant, by the ground state particle density  $n_o(\mathbf{r})$ .

**Theorem II:** A universal functional for the internal energy  $E[n]$  in terms of the density  $n(\mathbf{r})$  can be defined, valid for any external potential  $V_{ext}(\mathbf{r})$ . For any particular  $V_{ext}(\mathbf{r})$ , the exact ground state energy of the system is the global minimum value of this functional, and the density  $n(\mathbf{r})$  that minimizes the functional is the exact ground state density  $n_0(\mathbf{r})$ .

Let us briefly discuss these theorems without proving them. The first theorem states that the ground state of an interacting system is determined by the ground state electron charge density. From the external potential you can get, using the Schrödinger equation, the ground state many body wave function. Since the Hamiltonian is fully determined by the ground state density,  $n_o(\mathbf{r})$ , the number of variables is reduced to only three, as compared to  $3N$ , where  $N$  is the number of particles in the system. The second theorem states that for any external potential the total energy,

$$E[n] = F_{HK}[n] + \int V_{ext}(\mathbf{r})n(\mathbf{r})d\mathbf{r}, \quad (2.4)$$

can be expressed as the sum of a universal functional,  $F_{HK}[n]$ , of the interacting electron system and the external potential. Also the exact ground

state density is the density that minimizes the functional. However, the exact form of this functional is still not known.

## 2.4 Kohn–Sham ansatz

The Kohn–Sham ansatz [9] replaces the  $N$ -particle interacting problem with  $N$  one-particle non-interacting problems. In the Kohn–Sham ansatz the ground state density of the interacting system is assumed to be the same as that of the non-interacting system subjected to two potentials, namely the external potential,  $V_{ext}$ , and an exchange correlation potential,  $V_{xc}$ .

In the Kohn–Sham ansatz the ground state total energy is defined as,

$$E_0[n(\mathbf{r})] = T[n(\mathbf{r})] + \int V_{ext}(\mathbf{r})n(\mathbf{r})d\mathbf{r} + \frac{1}{2} \int \int \frac{n(\mathbf{r})n(\mathbf{r}')}{|\mathbf{r} - \mathbf{r}'|} d\mathbf{r}' d\mathbf{r} + E_{xc}[n(\mathbf{r})] + E_{II}, \quad (2.5)$$

where the first term is the kinetic energy of the non-interacting electrons, the second term is the electrostatic potential due to the nuclei, the third term is the Hartree energy, the fourth term,  $E_{xc}[n]$ , is the exchange–correlation energy which takes into account all non-classical interactions between electrons, and the last term,  $E_{II}$ , is the energy contribution from the nuclei–nuclei interactions. The Hartree term is the energy due to the interaction within a classical electron charge density distribution. The electrostatic repulsion in the Hartree energy is however overestimated. The overestimation of the Hartree energy is taken care of in the exchange–correlation term.

Using the fact that the total number of electrons is conserved,

$$n(\mathbf{r}) = \sum_{i=1}^N |\psi_i(\mathbf{r})|^2, \quad (2.6)$$

and using the variational principle leads to the one-particle Kohn–Sham equations,

$$\left( -\frac{\hbar^2}{2m_e} \nabla^2 + V_{KS} \right) \psi_i(\mathbf{r}) = \varepsilon_i \psi_i(\mathbf{r}), \quad (2.7)$$

where  $\psi_i$  is the Kohn–Sham orbitals and  $V_{KS}$  is,

$$V_{KS} = V_H + V_{ext} + V_{xc}. \quad (2.8)$$

In order to find the correct ground state electron density, the Kohn–Sham equations have to be solved in a self-consistent manner. The only part that we do not know how to obtain exactly is the exchange–correlation potential,  $V_{xc}$ . In the next section, we will discuss two approximations for the exchange–correlation.

## 2.5 Exchange–correlation functionals

The two most widely used approximations for the exchange correlation is the local density approximation (LDA) [9] and the generalized gradient approximation (GGA).

In LDA, the exchange–correlation energy is approximated with,

$$E_{xc} \approx E_{xc}^{LDA}[n] = \int n(\mathbf{r}) \epsilon_{xc}(n(\mathbf{r})) d\mathbf{r}. \quad (2.9)$$

In this approximation, the exchange–correlation energy in a specific point is being considered as the same as that of a locally uniform electron gas with the same density as in the specific point. Although this is a very crude approximation, which would not be expected to work very good when the electron density is quickly varying like in solids or molecules, experience have shown that this approximation works surprisingly well and has therefore been used extensively.

In an attempt to improve the exchange correlation energy, the GGA has been developed by also considering the gradient of the charge density. There are many different attempts at finding a good functional, the most commonly used functionals are those by Becke (B88) [10], by Perdew and Wang (PW91) [11] and by Perdew, Burke and Ernzerhof (PBE) [12].

## 2.6 Bloch electrons

The crystal potential displays a translational symmetry,

$$V_{ext}(\mathbf{r}) = V_{ext}(\mathbf{r} + n_1 \mathbf{a}_1 + n_2 \mathbf{a}_2 + n_3 \mathbf{a}_3), \quad (2.10)$$

where  $\mathbf{a}_i$  is the lattice vectors and  $n_i$  are integer numbers. Therefore, the Kohn–Sham orbitals can now be written,

$$\psi_{\mathbf{k}}(\mathbf{r}) = e^{i\mathbf{k} \cdot \mathbf{r}} u_{\mathbf{k}}(\mathbf{r}), \quad (2.11)$$

where  $\mathbf{k}$  is a vector in the first Brillouin zone,  $u_{\mathbf{k}}(\mathbf{r})$  a function with the periodicity of the lattice, and  $e^{i\mathbf{k} \cdot \mathbf{r}}$  a plane wave. This is known as the Bloch theorem [13], which reduces the problem from the large crystal to just a small part of it. The periodic function,  $u_{\mathbf{k}}(\mathbf{r})$ , can be expanded in a plane wave basis set as

$$u_{\mathbf{k}}(\mathbf{r}) = \sum_{\mathbf{G}} c_{\mathbf{k}} e^{i\mathbf{G} \cdot \mathbf{r}}, \quad (2.12)$$

where  $\mathbf{G}$  are the reciprocal lattice vectors. When equation (2.12) is inserted in equation (2.11), we get

$$\psi_{\mathbf{k}}(\mathbf{r}) = \sum_{\mathbf{G}} c_{\mathbf{k}, \mathbf{G}} e^{i(\mathbf{k} + \mathbf{G}) \cdot \mathbf{r}}. \quad (2.13)$$

To solve the KS equations using plane waves as a basis set is computationally demanding due to the large number of plan waves required to describe the wave functions. In the next section, we will discuss how the projector augmented-wave method can be used in order to lower the computational cost.

## 2.7 Projector augmented-wave method

The projector augmented-wave (PAW) [14] is a method for calculating the electronic structure. The PAW method combines features of the ultrasoft pseudopotential method [15] and the linear augmented-plane-wave method [16].

The wave function of the electrons are very different depending on whether the electron is close to the nucleus or far away in the bonding region. Within an atomic centred sphere, the augmented region, the PAW method uses a partial-wave expansion to describe the electrons. This is done because it is computationally heavy to represent the wave function with plane waves in the core region where the wave function oscillates rapidly. Outside the augmented region the electrons are described by plane waves or some other convenient basis set. The values and the derivatives of the function inside and outside the sphere is then matched.

The PAW method is based upon a transformation,  $\tau$ , from the all-electron wave function,  $\Psi$ , to a smooth pseudo wave function,  $\tilde{\Psi}$ ,

$$|\Psi\rangle = \tau|\tilde{\Psi}\rangle. \quad (2.14)$$

The pseudo wave function can be expanded into pseudo partial waves,

$$|\tilde{\Psi}\rangle = \sum_i c_i |\tilde{\phi}_i\rangle. \quad (2.15)$$

And the all-electron wave-function expanded as

$$|\Psi\rangle = \sum_i c_i |\phi_i\rangle. \quad (2.16)$$

The all-electron partial waves,  $\phi_i$ , are obtained from the solution of the radial Schrödinger equation for the isolated atom. Outside the augmented region, the pseudo partial waves and all-electron partial waves are equivalent. The transformation in (2.14) is linear and requires the pseudo partial waves  $|\tilde{\phi}_i\rangle$  to be dual to a projector function  $\langle\tilde{p}_i|$ , hence satisfying the condition

$$\langle\tilde{p}_i|\tilde{\phi}_j\rangle = \delta_{ij}. \quad (2.17)$$

Combining (2.15), (2.16) and (2.17) gives the transformation,  $\tau$ , now written as

$$\tau = \hat{\mathbf{1}} + \sum_i (|\phi_i\rangle - |\tilde{\phi}_i\rangle) \langle\tilde{p}_i|. \quad (2.18)$$

And if we write out equation (2.14) more explicitly

$$|\Psi\rangle = |\tilde{\Psi}\rangle + \sum_i (|\phi_i\rangle - |\tilde{\phi}_i\rangle) \langle \tilde{p}_i | \tilde{\Psi} \rangle. \quad (2.19)$$

The Kohn–Sham equation (2.7) can be written as

$$\tau^\dagger \hat{H} \tau |\tilde{\psi}_i\rangle = \varepsilon_p \tau^\dagger \tau |\tilde{\psi}_i\rangle. \quad (2.20)$$

Now the problem is computationally less demanding to solve than if just a plane wave basis set would have been used, since the number of plane waves required to give a good description of the Kohn–Sham orbitals will be much smaller.

## 2.8 Force theorem

The Hellmann–Feynman force theorem [17] can be used to find the global minimum energy structure of a system and to calculate the forces acting on the ions in *ab initio* molecular dynamics (AIMD), which will be described in the next chapter. If the atoms are not in their equilibrium positions, the total force acting on the atoms will be different from zero. The force can be calculated as

$$\mathbf{F}_I = -\frac{\partial E}{\partial \mathbf{R}_I}. \quad (2.21)$$

Combining equation 2.1 and 2.21, we can now write the force acting on the atoms as

$$-\frac{\partial E}{\partial \mathbf{R}_I} = -\left\langle \Psi \left| \frac{\partial \hat{H}}{\partial \mathbf{R}_I} \right| \Psi \right\rangle - \left\langle \frac{\partial \Psi}{\partial \mathbf{R}_I} \left| \hat{H} \right| \Psi \right\rangle - \left\langle \Psi \left| \hat{H} \right| \frac{\partial \Psi}{\partial \mathbf{R}_I} \right\rangle. \quad (2.22)$$

Due to the fact that the ground state energy is extremal to all possible variations of the wave function, the two last terms cancel out and we end up with,

$$\mathbf{F}_I = -\left\langle \Psi \left| \frac{\partial \hat{H}}{\partial \mathbf{R}_I} \right| \Psi \right\rangle = -\int n(\mathbf{r}) \frac{\partial V_{ext}}{\partial \mathbf{R}_I} d^3r - \frac{\partial E_{II}}{\partial \mathbf{R}_I}, \quad (2.23)$$

where the force is only depending on the electron density and the positions of the other nuclei.

### 3. *Ab initio* molecular dynamics

*The only reason for time is so that everything doesn't happen at once.*

— Albert Einstein

**M**OLECULAR DYNAMICS (MD) SIMULATIONS have been employed in order to take temperature and dynamical effects into account. In MD, the motions of the atoms are governed by the second law of Newton,

$$\mathbf{F}_i = m_i \mathbf{a}_i. \quad (3.1)$$

There are two types of molecular dynamic simulations, classical molecular dynamics (CMD) and *ab initio* molecular dynamics (AIMD). The difference between the two is how the force on the atoms,  $\mathbf{F}_i$ , is obtained. In the former the force is obtained from a model potential generated to mimic the behaviour of true atoms and in the latter case the forces are obtained from density functional theory calculations. The strength of CMD simulations is that because of the simple way the interactions between atoms are parameterized, CMD can be used to model large systems. However, there are limitations to the accuracy of the simulations because of the difficulty in creating good potentials which will correctly model all the underlying physics, *e.g.* charge transfer is difficult to simulate using CMD. In *ab initio* MD, the biggest limitation is the computational cost. The long computational time required to calculate the forces practically limits the simulations to a few hundreds of atoms, several orders of magnitude smaller as compared to what is computationally possible within CMD.

In the following sections, a short introduction to Born–Oppenheimer MD, the equilibration of MD simulations, and a set of tools to analyze MD results will follow.

#### 3.1 Born–Oppenheimer molecular dynamics

In AIMD, we always have two parts to solve, the motion of the nuclei and the calculation of forces from the self-consistent solution of the Kohn–Sham equations. In Car–Parrinello MD [18], a fictitious dynamics of the electrons is introduced in order to solve the dynamics of the nuclei and the quantum mechanical problem of the electrons, calculation of the atomic forces, on the same footing. In Born–Oppenheimer molecular dynamics, the calculation

of the forces acting on the atoms and the motion of the nuclei are treated separately. The nuclei move according to the solution of Newton's equation and the forces acting on the nuclei are calculated from the electronic structure while the atoms are kept at fixed positions.

## 3.2 Equilibration

*Ab initio* molecular dynamics is computationally a heavy task. For this reason it is important to know what timescale is needed for the MD simulations. When a MD simulation is started, usually the atomic velocities are assigned randomly. This will result in oscillations in the total energy and the distributions of velocities and forces which are non-physical. After running the simulations for a while, these un-physical oscillations will subside. In order to know after what length of time the data from the molecular dynamics simulation can be used for analysis, it is important to determine when the simulation is equilibrated. This can be done by looking at the convergence of properties like total energy, forces, velocities and atomic positions. We have developed an equilibration function,  $c(t)$ , which we defined as

$$c(t) = \sum_{\Delta t=0}^{t_{d-max}} \sum_{n=1}^N (A_n(t) - A_n(t + \Delta t))^2, \quad (3.2)$$

where  $A_n$  is the studied property,  $N$  is the total number of atoms,  $t$  is the time, and  $t_{d-max}$  is the maximum time difference in which to check for change in the studied property. The equilibration function will only be defined in the time ranging from  $t = 0$  to  $t_{tot} - t_{d-max}$ , where  $t_{tot}$  is the total time of the simulation. The length of  $t_{d-max}$  is usually set to half of the simulation time since a larger value will give a better confidence that the equilibration has been reached. However, if the equilibration point is reached after the time  $t_{tot} - t_{d-max}$  the equilibration point can not be seen in the equilibration function. It should also be noted that if a global property of the system like the total energy is studied for convergence, then there will be no summation (Equation 3.2) over the atoms. In Figure 3.1 a typical equilibration function is shown. Here it can be seen that the velocity distribution of this system is equilibrated after about 1.2 ps.

## 3.3 Radial distribution function

In order to analyze the data obtained from MD, there is a set of tools which will be briefly explained in the following sections.

Radial Distribution Functions (RDF) can be obtained either from experiments, using *e.g.*, x-ray scattering or neutron scattering, or from molecular dynamics simulations. In MD, we are not limited to calculating

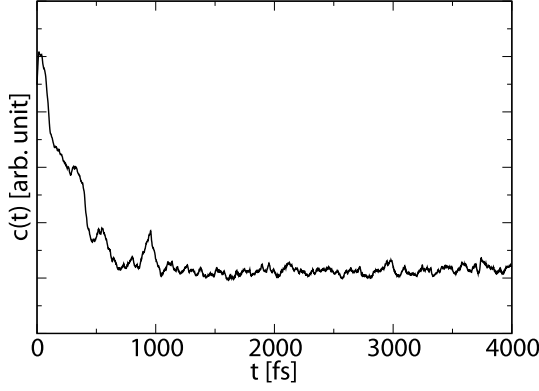


Figure 3.1: A typical equilibration function for the velocity distribution in a MD simulation.

the total RDF, but can also calculate partial RDFs where the contribution of different elements are split up.

The RDF is defined as

$$g(r) = \frac{1}{N} \sum_{l=1}^N \frac{N_l(r)}{\rho \, 4\pi \, r^2 \, \Delta r}, \quad (3.3)$$

where  $\rho$  is the average density of the system,  $N$  is the total number of atoms, and  $N_l(r)$  is the number of atoms found within the spherical shell with a radius larger than  $r$  and smaller than  $r + \Delta r$  centred on atom  $l$ . The RDF is calculated summing over all the atomic positions as the sphere-centres.

The RDF can be used to study changes in the local atomic environment, number of neighbours, and if a system is crystalline, amorphous, or molten. For example, in a transition from a *hcp* to an *fcc* phase, the number of nearest-neighbours will remain twelve but the next-nearest-neighbours will change from eight to six. In the RDF, this transition can be seen from the integration of the first and second peaks. If the system turns into a liquid, the long range correlation in the RDF will disappear and the RDF will become smoother.

### 3.4 Mean square displacement

From the Mean Square Displacement (MSD) information about melting can be obtained. The MSD is calculated in the following way,

$$\langle |\mathbf{r}(t) - \mathbf{r}(0)|^2 \rangle = \frac{1}{N} \sum_{t_0=0}^{t_d-\max} \sum_{n=1}^N |\mathbf{r}_n(t_0) - \mathbf{r}_n(t_0 + t)|^2, \quad (3.4)$$

where  $\mathbf{r}_n(t_0)$  is the atomic position of atom  $n$  at a time  $t_0$  and  $\mathbf{r}_n(t_0 + t)$  the position at a time  $t$  from time  $t_0$ . The starting time  $t_0$  is then moved in steps

from the beginning of the simulation to a time,  $t_{d-max}$ , which is usually half the simulation length, in order not to favour one specific configuration and to gain more statistics. The MSD is normalized with the number of atoms,  $N$ , and number of time intervals,  $N_{t_0}$ , used in the averaging.

The atomic diffusion coefficients can be calculated from the MSD data. In the linear regime of the MSD, the following equation can be fitted to the data

$$\langle |\mathbf{r}(t) - \mathbf{r}(0)|^2 \rangle = 6 D t + C, \quad (3.5)$$

where  $C$  and  $D$  are constants. Here, the constant  $D$  is the Einstein diffusion coefficient. The diffusion coefficient tell you how long distance, in average, an atom will travel during a given time. If a phase-transition occurs during the simulation, there is a risk of getting an artificially high diffusion coefficient. The artificially high diffusion is due to the spacial movement of atoms from one phase to the other. This can be seen if a MSD curve, after the initial part, starts out with one finite slope and then after a while changes to a smaller or no slope.

### 3.5 Residence time

A different method to calculate the diffusion coefficient is by using the average residence time of the diffusing atoms.

$$D = \frac{1}{6} \frac{l^2}{\langle \tau \rangle}, \quad (3.6)$$

where  $l$  is the jump distance and  $\langle \tau \rangle$  is the average site residence time. The advantage of this approach, compered to MSD, is that the requirement for jump statistics will be lower. The disadvantages is that you need to define the sites between which the atom jumps.

### 3.6 Bond angle distribution

To probe the local atomic structure, the bond angle distribution (BAD) can be used. The BAD gives information about what the angles are in between the nearest-neighbours.

$$g(\theta) = \sum_{n=1}^N N_n(\theta), \quad (3.7)$$

where  $N_n(\theta)$  is the number of atoms with the an angle  $\theta$  between the nearest-neighbours. As an example, in a perfect diamond structure there will be only one peak at  $109.5^\circ$ , corresponding to the tetrahedral angle between the nearest-neighbours. As the temperature is added, the sharp peak will broaden.

If there is a phase transition to another geometry, this can be seen from a change in the BAD peaks.

### 3.7 Bond orientation distribution

Bond orientation distribution (BOD) is similar to BAD. In BAD, the nearest-neighbour was used as a reference. In BOD, a fixed orientation, *e.g.* a lattice vector, is used as the reference frame. This can be useful when looking at how different bonds are behaving with respect to the lattice. Order to disorder transitions can be seen in this way.

### 3.8 Vibrational spectral density

From the MD simulation, we can obtain the velocity auto-correlation function (VACF),  $\Phi(t)$ , defined by

$$\Phi(t) = \frac{1}{N N_{t_0}(t)} \left\langle \sum_{t_0=0}^{N_{t_0}(t)} \sum_i^N \mathbf{v}_i(t_0) \cdot \mathbf{v}_i(t_0 + t) \right\rangle, \quad (3.8)$$

where  $\mathbf{v}_i$ ,  $t$ ,  $N$ , and  $N_{t_0}(t)$  is the velocity of atom  $i$ , the time, the number of atoms in the system, and the number of  $t_0$  for time  $t$ , respectively.

A value  $\Phi(t) = 1$  means that the system velocities have the same direction and amplitude after time  $t$ , and oppositely, a value  $\Phi(t) = -1$  means that the system is anti-correlated, *i.e.* the velocities are the exact opposite after time  $t$ . The VACF provides information on what timescale there is correlation of motion in a system: (i) in a gas, the VACF has an exponential decay, (ii) in a liquid it decays as  $t^{-d/2}$  [19], where  $d$  is the dimensionality of the system, (iii) while for a crystalline solid the correlation has a long lifetime.

The vibrational spectral density (VSD),  $I(\omega)$ , can be obtained by taking the Fourier transform of the VACF,

$$I(\omega) = \int_0^\infty e^{i\omega t} \Phi(t) dt. \quad (3.9)$$

The VSD gives information of the atomic vibrations, and in section 4.4.2, it is demonstrated how the VSD can be used to compare bond strengths.



## 4. Diffusion

*Ludwig Boltzmann, who spent much of his life studying statistical mechanics, died in 1906 by his own hand. Paul Ehrenfest, carrying on the work, died similarly in 1933. Now it is our turn to study statistical mechanics.*

— David L. Goodstein

THE KINETICS OF A CHEMICAL PROCESS, involving solid state reactants, can be divided into two contributions, namely mass transport and surface reaction barriers. Mass transport, hereafter denoted diffusion, is one of the key properties in many materials today. Either a high diffusion is desirable, *e.g.* in batteries, fuel cells, and storage materials, or the blocking of diffusing species, *e.g.* in material put under extreme conditions.

### 4.1 Diffusion mechanism

The mechanism of the diffusion is determined by the temperature region. Possible diffusion mechanisms, starting from low temperatures, as shown in Figure 4.1, are:

- coherent tunnelling
- incoherent tunnelling, or phonon-assisted tunnelling
- classical over barrier jump

In the two first cases, the diffusion is mediated through the quantum wave nature of the particle. The difference between coherent and incoherent tunnelling, is whether phonons are required to align the energy levels of the sites along the diffusion path, or not.

The main focus of this chapter will be classical jump diffusion.

### 4.2 Classical jump diffusion

Diffusion between sites can be described as an activated process with a diffusion barrier in between two sites (see Figure 4.1). The Arrhenius equation,

$$k(T) = Ae^{-E_a/k_B T}, \quad (4.1)$$

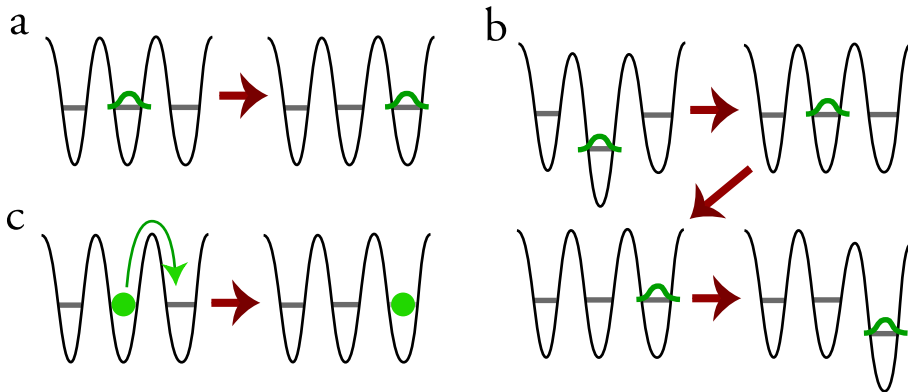


Figure 4.1: (a) Coherent tunnelling, (b) phonon-assisted tunnelling, and (c) classical over barrier jump

where  $A$  is a constant,  $E_a$  is the activation energy, and  $k_B$  is the Boltzmann constant, can be used as an empirical relationship between temperature,  $T$ , and diffusion rate,  $k(T)$ . The activation energy in classical diffusion is the barrier height between two sites, as illustrated in Figure 4.1c.

#### 4.2.1 Transition state theory or molecular dynamics

Molecular dynamics can be used to study diffusion processes in great detail, including dynamical effect. However, if the thermal energy is much smaller than the barrier height, the required simulation time might be too large to be feasible. Instead we may turn to a different field of statistical physics. In the following, a short introduction to Transition State Theory (TST) will be given.

#### 4.2.2 Harmonic transition state theory

In TST the diffusion rate is calculated by finding the transition state between a reactant state, the starting site of the diffusing species, and a product state, the result site after a successful jump. The rate constant is obtained from,

$$k_{TST}(T) = \sqrt{\frac{k_B T}{2\pi m}} \frac{Z_{TS}}{Z_R}, \quad (4.2)$$

where  $m$  is the mass of the diffusing entity,  $Z_R$  the partition function of the reactant state, and  $Z_{TS}$  the partition function of the transition state.

In many solids, we can use the harmonic approximation to simplify the problem. The limitations of the harmonic approximation are the following: *pro primo* difference in energy between the reactant state and a first order saddle point (one imaginary frequency) must be larger than  $5k_B T$ , *pro secundo* the difference between a first order and a second order saddle point (two imaginary frequencies) must be larger than  $k_B T$ . In harmonic transition state

theory (HTST), the rate constant is given by,

$$k_{HTST}(T) = \frac{\prod_i^D v_i^R}{\prod_i^{D-1} v_i^{SP}} e^{-(V_{SP}-V_R)/k_B T}, \quad (4.3)$$

where we now have the real vibrational frequencies,  $v^R$  and  $v^{SP}$ , of the reactant state and the saddle point, respectively.  $V_{SP} - V_R$  is the difference in potential energy between the two states.

Zero-point energy (ZPE) effects arise from the fact that the ZPE is not the same in the reactant state as in the transition state. In order to account for this we can use the quantum mechanical partition function, instead of the classical. This "quasi-quantum" approximation (QQ-HTST) gives the rate,

$$k_{QQ-HTST}(T) = \frac{k_B T}{2\pi\hbar} \frac{\prod_i^D 2\sinh(hv_i^R/2k_B T)}{\prod_i^{D-1} 2\sinh(hv_i^{TS}/2k_B T)} e^{-(V_{SP}-V_R)/k_B T}, \quad (4.4)$$

where ZPE-effects now are included in the prefactor.

In the following, we will first have a look at diffusion of hydrogen in transition metals, and later diffusion of lithium in Li-N-H systems.

## 4.3 Hydrogen diffusion in transition metals

Metal-hydrogen systems serves as a prototype for the lattice gas models. Due to the simplicity of the resulting changes in the electronic structure, hydrogen in metals can also be viewed as the most simple obtainable class of alloys. In the classical limit, where quantum effects can be ignored, the diffusion rate of hydrogen is experimentally well established for most metals [20–23].

In Figure 4.2, our calculated diffusion constants for V, Nb, and Ta is plotted alongside experimental values from the literature. As can be seen, HTST gives reasonable agreement with experimental values in the temperature region where classical jump diffusion should be the dominating diffusion mechanism. At lower temperatures, the QQ-HTST, which includes zero-point energy effects does a better job, but the agreement is still poor. The reason is that tunnelling effects, which are important at low temperatures, are not accounted for.

### 4.3.1 Effects of self-trapping on diffusion in Nb

In Paper I, we have investigated the dynamical effects of self-trapping on the high temperature classical jump diffusion of hydrogen in Nb using AIMD. When a hydrogen atom is absorbed in a transition metal, it attracts and localizes some of the neighbouring metal d-electrons and as a consequence the interatomic metal binding diminishes [26, 27]. The interstitial hydrogen thereby gives rise to a local strain field, which decays as  $r^{-2}$  where  $r$  is the distance from the hydrogen atom [22]. The displacement of the lattice in response to the interstitial hydrogen causes large changes in the energy

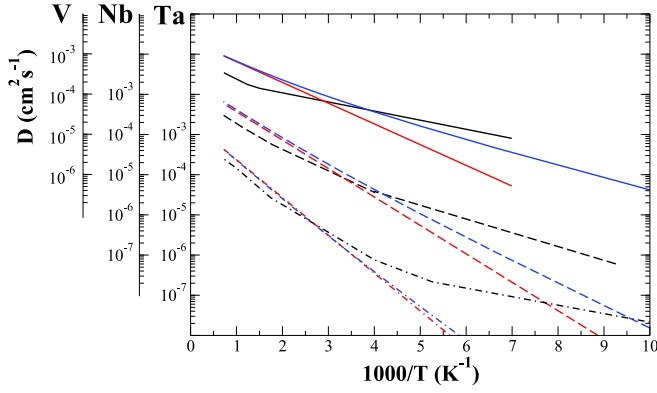


Figure 4.2: Arrhenius plot of the calculated and experimental diffusion coefficients for V (top, solid lines), Nb (middle, dashed lines), and Ta (bottom, dashed-dotted lines). The experimentally rates from the literature are drawn in black [24, 25], HTST (without ZPE-effects) is drawn in red, and QQ-HTST (with ZPE-effects) is drawn in blue.

landscape, called the self-trapped state and has been determined theoretically, using empirical potentials, in niobium by Fukai to 0.475 eV [26], and by Li and Wahnström to 0.30 eV [28]. Using *ab initio* methods, Sundell and Wahnström calculated the self-trapping energy to 0.189 eV [29, 30]. The effect of self-trapping on the energy landscape is illustrated in Figure 4.3.

The interstitial hydrogen and its associated displacement field can be regarded as a quasi-particle and is often referred to as the small-polaron, or lattice polaron, in analogy with the electron polaron in dielectric materials [31–33]. The polaron has an effective mass that depends on the displaced metal atoms and is typically much larger than the mass of the interstitial hydrogen. The diffusion of hydrogen in metals therefore involves two entities: the light interstitial and the strain field. Thus, although the Arrhenius description can be used to reproduce diffusion rates at elevated temperatures, the conceptual basis for it can be said to be incomplete. We have addressed this issue using *ab initio* molecular dynamic calculations, including the diffusion of both the interstitial and the corresponding local strain field.

In the dilute  $\alpha$  phase, hydrogen occupies tetrahedral sites of the bcc Nb in a random configuration [21, 22], which is in good agreement with the isosurface of the hydrogen density obtained from the simulations at 550 K shown in Figure 4.4.

The energy landscape of a hydrogen atom self-trapped at a tetrahedral site is illustrated in Figure 4.3. The potential far away from the hydrogen atom, describing the potential in the absence of self-trapping, is shown in the upper left. The energy of the surrounding sites can be obtained at 0 K, by moving the proton to different sites while keeping the lattice, including the self-trapped state, frozen. Tracing the energy of the T-sites yields the potential seen by instantaneous hopping of hydrogen and we define the resulting energy landscape as the excited states of the quasi-particle. The blue

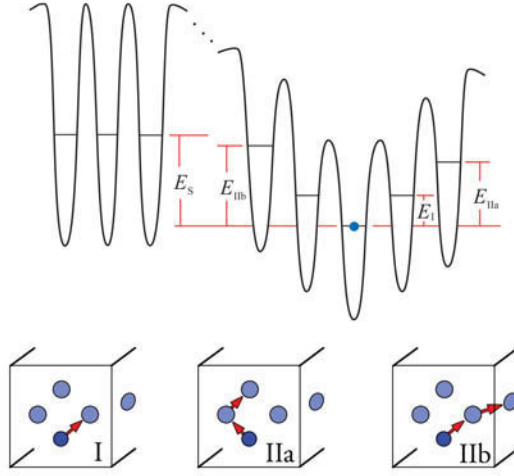


Figure 4.3: The self-trapping lowers the hydrogen–polaron quasi–particle energy level,  $E_S$ , with respect to the unstrained lattice.  $E_I$  is the difference in energy when moving the hydrogen to the closest tetrahedral site, keeping the position of the strain field fixed with respect to the lattice.  $E_{IIa}$  and  $E_{IIb}$  are similarly the energies for moving the hydrogen to the next nearest tetrahedral sites. The geometries of the jumps are shown in the bottom panel.

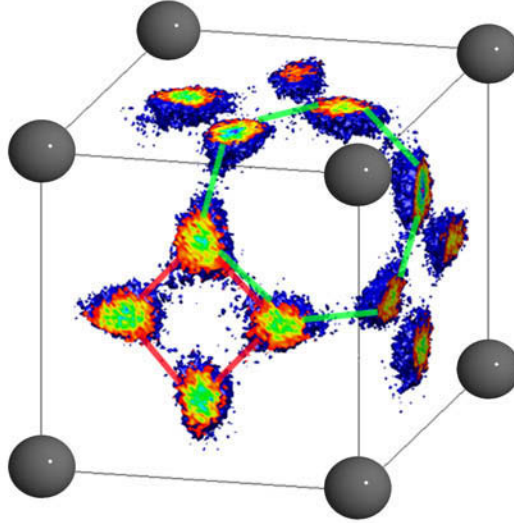


Figure 4.4: An iso–surface of the hydrogen density in bcc Nb at 550 K. Notice how the points cluster around the tetrahedral sites in excellent agreement with experimental results [21]. The red and green lines shows the 4T and 6T rings of interstitial tetrahedral sites, respectively. The grey spheres are Nb atoms.

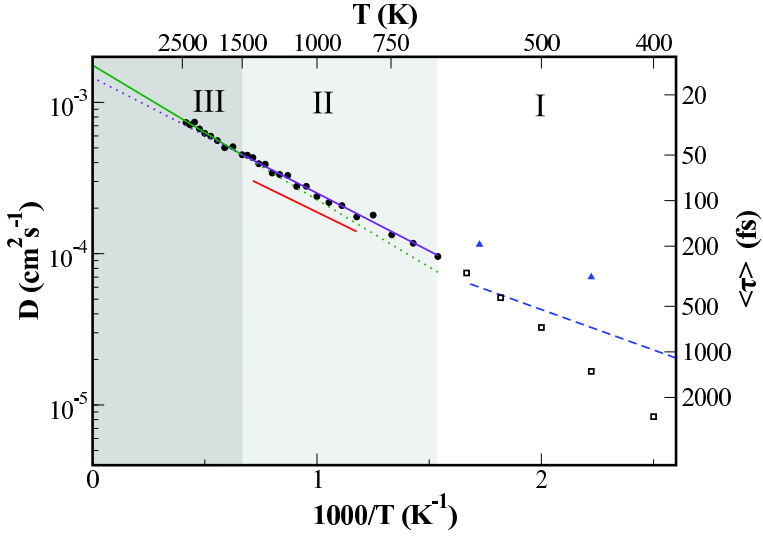


Figure 4.5: Arrhenius plot of the calculated and experimental diffusion coefficients. The black circles and squares show our calculated diffusion rates. The experimentally obtained rates are drawn in red (solid)[24] and blue (dashed) [25]. The blue triangles are results obtained from classical MD [34].

point symbolizes the proton in its self-trapped state, and the corresponding self-trapping energy is denoted by  $E_S$ . Three cases are considered in the lower panel of Figure 4.3: a jump from the self-trapped site to one of the nearest tetrahedral sites on the 4T ring resulting in an energy difference  $E_I = 0.071$  eV, a double jump process on the 4T ring, denoted as IIa with the energy  $E_{IIa} = 0.148$  eV, and a double jump on the 6T ring, giving  $E_{IIb} = 0.189$  eV is denoted as IIb. These energies describe the energy landscape within the polaron, and should not be confused with activation energies for hydrogen diffusion, since the energies correspond to differences between energy levels, not barrier heights, and the potential is dynamic. The equilibrium self-trapped energy at 0 K was determined to be  $E_S = 0.206$  eV including ZPE and 0.170 eV without ZPE, which is in agreement with the results of Sundell and Wahnström (0.189 eV) [29, 30]. The calculated self-trapping energy is significantly smaller than the results obtained from empirical model calculations by Fukai (0.475 eV) [26], and by Li and Wahnström (0.30 eV) [28].

The diffusion coefficients were calculated from the mean residence time of hydrogen,  $\langle \tau \rangle$ , [22] in the temperature range 400 K to 2400 K and the results are plotted in Figure 4.5.

The activation energies in region II and III are 0.151(4) eV and 0.176(5) eV, respectively. No experimental results are available for temperatures corresponding to region III in the figure, while the results in region II are in excellent agreement with the experimental data, 0.144(3) eV [24]. In region I, the agreement is less compelling. The limited cell size will cause an artificial polaron self-interaction, through the periodic boundary

conditions. Using the cell size (10 Å) and the speed of sound in Nb (34 Å/ps) we determined the characteristic interaction time to be 300 fs, which agrees well with 600 K as a crossing point.

Now let us consider the effect of self-trapping on the local strain of the niobium lattice. We have used the first peak of the H–Nb radial distribution function as a measure of the amplitude of the local strain field (H–Nb distance) in the immediate vicinity of the interstitial. In the hydrogen-free niobium lattice, the distance from the interstitial tetrahedral site to the four closest Nb atoms was determined to be 1.86 Å at 0 K, in excellent agreement with the literature. When an H atom is placed in this tetrahedral site, the distance increases to 1.96 Å at 10 K. By plotting (Figure 4.6) this distance as a function of temperature we can follow the changes in the amplitude of the local strain field. The results displayed in Figure 4.6 are obtained from simulations performed at a constant volume. Ignoring the thermal expansion eased the calculations and the extraction of the hydrogen induces changes in the atomic distances. This approach is motivated by the negligible influence of the volume on the difference in the H–Nb distances at different residence times, which was verified by 900 K and 1500 K simulations with different volumes of the cell. As seen in the figure, the average distance exhibits a close to linear decrease with increasing temperature to approximately 1000 K where it levels out. This result resembles the average changes in the lattice displacement for all residence times ( $\tau$ ). It is also worth noting that the distance does not reach 1.86 Å, which is the distance in the hydrogen free lattice. Thus, a local strain field is always present, while its amplitude and distribution depends on the temperature.

Furthermore, analyzing the jump angles we find that the distribution of probabilities for different angles is temperature dependent. Wahnström and Li [34] found from their analysis of the jump angles at 450 K that the proportion of jumps back to the last occupied T-site is much larger in comparison to what would be expected from an uncorrelated sequence of random jumps. The over representation of jumps back to the last occupied T-site can be understood from the difference in energy levels as shown in Figure 4.3. Immediately after the jump between T-sites, the polaron is in an excited state. The de-excitation has two possibilities, return to the initial T-site, *or* a translation of the local strain field. The upper limit for the excitation of the polaron is defined by the self-trapping energy of the hydrogen. The internal excitation of the polaron results in an increased activation energy, which is consistent with experiments as well as our findings.

The increase of the hopping rate with increasing temperature, combined with the temperature independent relaxation time of the lattice, results in an unbinding of the hydrogen strain field pair. As a consequence, the amplitude of the local lattice displacement must depend on  $\tau$ . To prove this point, we plot, in Figure 4.6, the H–Nb distance obtained for  $\tau \leq \langle \tau \rangle$ , as a function of temperature. The choice of time scale is somewhat arbitrary, but serves the purpose of separating the long and short residence times. As seen from Figure 4.6, the mean displacement, and the displacement developed around

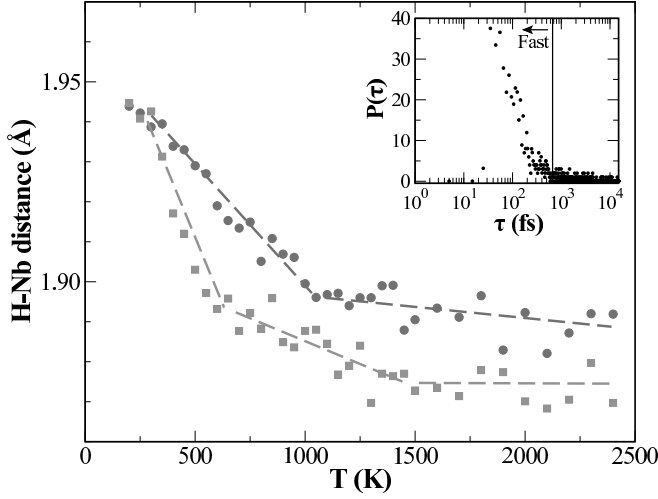


Figure 4.6: The average distance between hydrogen and the nearest neighbour Nb as a function of temperature (circles). The probability of residence,  $P(\tau)$ , as a function of residence time ( $\tau$ ), at 500 K, is illustrated as an inset. The squares show the H-Nb distance for residence times smaller than the average residence time,  $\langle \tau \rangle$ .

the fastest moving hydrogen, is the same at and below room temperature. Thus, at these temperatures, the proton and the strain field are fully coupled and diffuse as a unity (polaron diffusion). Above room temperature, we can see a difference in the strain field amplitude depending on whether the protons have long or short residence times.

Above 1500 K the change in displacement with temperature is weak, which we interpret as the limit of the unbinding between the proton and the strain field. Therefore, this temperature serves as a natural dividing line between regions II and III in Figure 4.5. A distinct difference in the activation energies is seen between these two regions, 0.151(4) eV in region II and 0.176(5) eV in region III. We note that a partial self-trapped state is still found at the highest temperatures, as the displacement is not the same for all  $\tau$ . Thus, the unbinding of the polaron is not complete, even at the highest temperatures. We did not detect any stress dependence on the proton residence time, from an analysis of the cell stress. This implies that even though the local strain field around the proton diminishes, the global strain field does not, *i.e.* there must be a strain field trail following the diffusing hydrogen.

In conclusion, we have demonstrated a temperature dependent unbinding of the proton and its local strain field. At elevated temperatures this effect results in a strain field trail, reflecting the diffusion trace of the interstitial.

When reinterpreting the experimental results [24, 35–37], on the basis of our findings, the importance of the relaxation time of the lattice on the hydrogen diffusion becomes apparent. Internal excitations within the polaron are a consequence of the short time scale of the dynamics of the light interstitial, as compared to the relaxation time of the lattice. This will

influence the H–H interaction and is expected to be of large importance for understanding the collective dynamic behaviour, such as order/disorder transitions, in all transition metal–hydrogen systems.

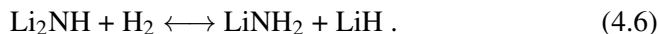
## 4.4 Lithium diffusion

In this section, we shall discuss our results for the coexistence of solid and quasi–liquid sublattices in  $\text{Li}_2\text{NH}$ , Paper II, the difference in diffusion mechanisms between  $\text{Li}_3\text{N}$ ,  $\text{Li}_2\text{NH}$ , and  $\text{LiNH}_2$ , Paper III, and finally between  $\alpha$ – and  $\beta$ – $\text{Li}_3\text{N}$ , Paper IV. Solid–state systems possessing a high mobility of lithium ions are of tremendous interest for battery and fuel cell applications. As a consequence, the research into new materials with high lithium ion conductivity forms a very active field. Lithium nitride ( $\text{Li}_3\text{N}$ ) is one such material in which lithium ions are known to exist in a highly mobile superionic state. Hydrogenation of this system leads to the formation of lithium imide [38] ( $\text{Li}_2\text{NH}$ ) and subsequently of lithium amide [39] ( $\text{LiNH}_2$ ), a process which has been proposed [40] and further investigated [41–49] for its merits in the field of hydrogen storage research [3, 50–56].

Chen *et al.* [40] showed that it is possible to store up to 11.5 wt% of hydrogen in solid–state Li–N–H systems through the following reversible reactions:



and



These findings have prompted a flurry of investigations both from experimentalists and theoreticians [41–47] into  $\text{LiNH}_2$  and  $\text{Li}_2\text{NH}$ , two compounds which had been known since the 1950s [38, 39]. In particular for  $\text{Li}_2\text{NH}$ , a vivid discussion was carried out in the literature about its correct low– and high–temperature structure. Our contribution to this discussion, aim to reach a better understanding of the transition that apparently takes place from the low– to the high–temperature phase.

### 4.4.1 Li diffusion in Li–N–H systems

Experimental results show a temperature–induced order–disorder structural phase transformation that occurs in  $\text{Li}_2\text{NH}$  at about 385 K. In Paper II we have employed AIMD in an attempt to study this transition. A structural phase transition was observed by us in the temperature range 300–400 K, in good agreement with experiment. This transition is associated with a melting of the cation sub–lattice ( $\text{Li}^+$ ), giving rise to a superionic phase, which in turn is accompanied by an order–disorder transition of the N–H bond orientation distribution. In Paper III we show from first principles that the step–wise addition of hydrogen to  $\text{Li}_3\text{N}$  can act both as a promoter and inhibitor of the

superionic state. Furthermore we investigate the detailed diffusion mechanism in all three materials.

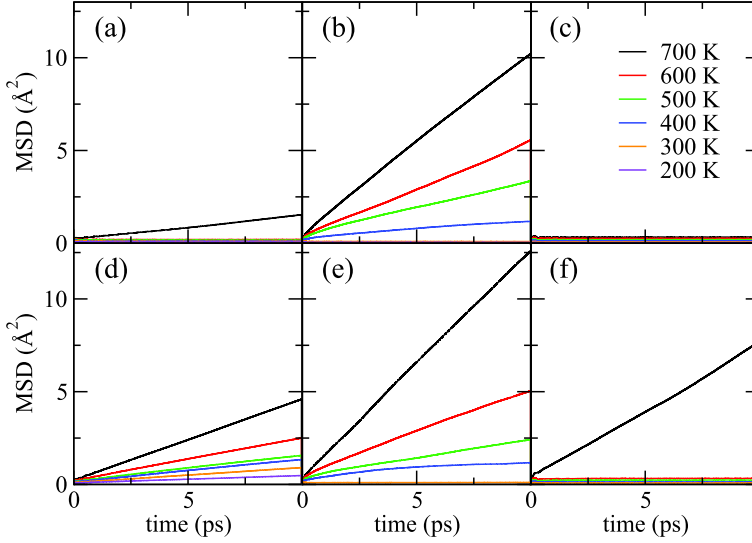


Figure 4.7: Mean square displacement for Li ions as a function of time in (a)  $\text{Li}_3\text{N}$ , (b)  $\text{Li}_2\text{NH}$ , and (c)  $\text{LiNH}_2$  with *no* Li vacancies. MSD with *one* Li vacancy in the supercell in (d)  $\text{Li}_3\text{N}$ , (e)  $\text{Li}_2\text{NH}$ , and (f)  $\text{LiNH}_2$ . Note that the scale on the y-axis is identical in all six panels to facilitate comparisons.

The temperature-dependent mean square displacement for Li ions in  $\text{Li}_3\text{N}$ ,  $\text{Li}_2\text{NH}$ , and  $\text{LiNH}_2$  is plotted as a function of time in Figure 4.7. Zero-slope MSD curves indicate that Li stays essentially bound to its equilibrium site, with the finite height of the MSD level attributed to the ion's vibrational amplitude, which is seen to rise with temperature. A finite-slope MSD curve is the telltale sign of diffusion taking place. Thus, in the case of  $\text{Li}_3\text{N}$  (Figure 4.7a), it is clearly observed from the flat MSD curves for  $T=200\text{--}600\text{ K}$  that Li does not become mobile until the temperature has reached 700 K. For  $\text{Li}_2\text{NH}$  on the other hand, Li starts diffusing already at a comparatively low temperature of 400 K (Figure 4.7b). Finally, for  $\text{LiNH}_2$ , we find absolutely no mobility of Li in the studied temperature range (Figure 4.7c). It is important to note that for all three systems, the nitrogen atoms remain fixed to their respective equilibrium sites throughout the studied temperature range. Thus, in those cases where Li becomes mobile, the system is truly in a superionic state.

Analogous to electron or hole migration in semiconductors, the diffusing species can either be a particle or a vacancy. Particle diffusion requires a structure with open space where the particle can diffuse. Vacancies can be created in three different ways: (i) Frenkel defects, (ii) non-stoichiometric growth conditions, and (iii) applying an electric field to pull ions out of the material.

In order to investigate the effects of vacancies on the diffusion, we have also carried out MD simulations with Li–vacancies present in all three materials. It should be noted that the vacancy concentration will have a big influence on the magnitude of the diffusion; here, however, we are only interested in whether vacancies affect the diffusion or not. As can be seen from Figure 4.7d, a Li vacancy in  $\text{Li}_3\text{N}$  allows for the diffusion to start already below room temperature. In  $\text{Li}_2\text{NH}$ , there is virtually no effect on the MSD when introducing a Li vacancy (Figure 4.7e), and no change in allowed temperature range for the diffusion can be observed from the coarse set of temperatures in our simulations. In  $\text{LiNH}_2$  with one Li vacancy, we notice diffusion starting at a temperature of 700 K (Figure 4.7f). These results can be interpreted as follows: the Li sub–lattices in  $\text{Li}_3\text{N}$  and  $\text{LiNH}_2$  require vacancies in order to allow for Li diffusion, while in  $\text{Li}_2\text{NH}$ , vacancies are apparently not a requirement.

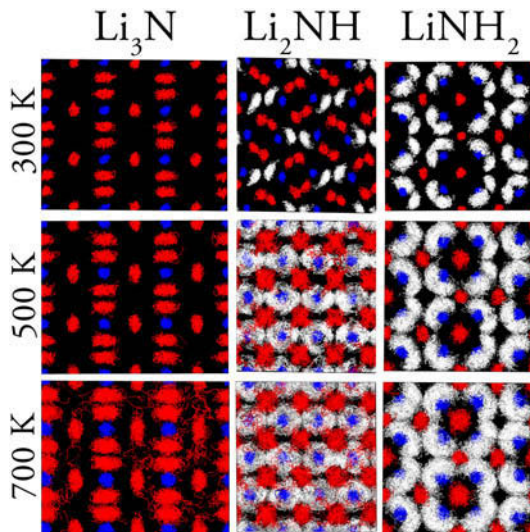


Figure 4.8: Ion trajectories in  $\text{Li}_3\text{N}$ ,  $\text{Li}_2\text{NH}$ , and  $\text{LiNH}_2$ , projected into the  $yz$  plane for 300 K, 500 K and 700 K. The horizontal axis is aligned with the  $[001]$  direction while the vertical axis aligns with  $[010]$ . Trajectories are coloured red, blue and white for Li, N, and H, respectively.

Figure 4.8 displays a visualization of the ion trajectories from our MD simulations for the systems in which *no* Li vacancy has been introduced.

The trajectories plot also shows how the hydrogen atoms in  $\text{Li}_2\text{NH}$  and  $\text{LiNH}_2$  possess a clear orientational preference at low temperatures, but as the temperature rises, they are seen to explore an increasingly larger space around the nitrogen atoms to which they are respectively bound. This behaviour is actually even better captured in the form of a bond orientation distribution graph, shown in Figure 4.9. As can be seen, in the case of  $\text{Li}_2\text{NH}$  at 200 K and 300 K, the N–H bonds deviate only very slightly from their zero–temperature orientation. But coinciding with the onset of Li diffusion at 400 K, the bond

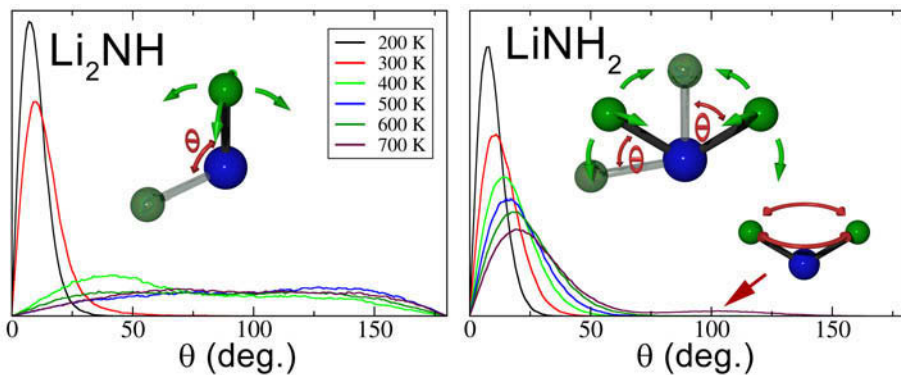


Figure 4.9: Bond orientation distribution plot for N–H bonds in  $\text{Li}_2\text{NH}$  (left panel) and  $\text{LiNH}_2$  (right panel). The distribution shows, for a given temperature, the deviation of N–H bond orientation from their respective 0 K orientation. The respective insets illustrate the definition of  $\theta$ , with the solid structures referring to the 0 K orientation and the slightly transparent one to an arbitrary example of a finite-temperature orientation (N in blue and H in green). It also worth noting that in the case of  $\text{LiNH}_2$ , the slight elevation of the 700 K curve at around  $100^\circ$  corresponds to an exchange between the two N–H bonds in the  $\text{NH}_2$  unit as illustrated in the second inset of the right panel.

orientation distribution changes drastically, indicating that the N–H bonds rotates freely. For  $\text{LiNH}_2$ , the individual N–H bonds of the  $\text{NH}_2$  units remain within close vicinity of the zero-temperature orientation (Figure 4.9), merely vibrating back and forth within a confined angular range. It thus seems that the full rotation of N–H bonds in  $\text{Li}_2\text{NH}$  is strongly linked to the promotion of Li mobility, while the absence of bond rotation in  $\text{LiNH}_2$  is seen to be connected to the inhibition of Li mobility.

The presented findings can then be summarized and interpreted as follows. In  $\text{Li}_3\text{N}$ , the diffusion is controlled by the concentration of vacancies. In  $\text{Li}_2\text{NH}$ , the diffusion is independent of vacancies, and is initiated at the same temperature, 385 K, as the rotation of N–H bonds. In  $\text{LiNH}_2$  the diffusion is blocked until 700 K, where it is controlled by vacancies.

#### 4.4.2 Vibrational spectra of Li–N–H systems

From the AIMD simulations performed for the Li–N–H systems, we can get the VSD to get further information on the dynamic interaction between the different atomic species. In Figure 4.10, the VSD is plotted. The first thing that we see is that the bands of vibration of the elements is in the inverse order of mass. Because hydrogen is lighter than both Li and N, we expect it to follow the motion of the other species, as is seen in the region below 30 THz for the H atoms. The N–H vibrations are seen as peaks at  $\sim 96$  THz in  $\text{Li}_2\text{NH}$  and  $\sim 102$  THz in  $\text{LiNH}_2$ . This indicates that the N–H bond is stronger in  $\text{LiNH}_2$ .

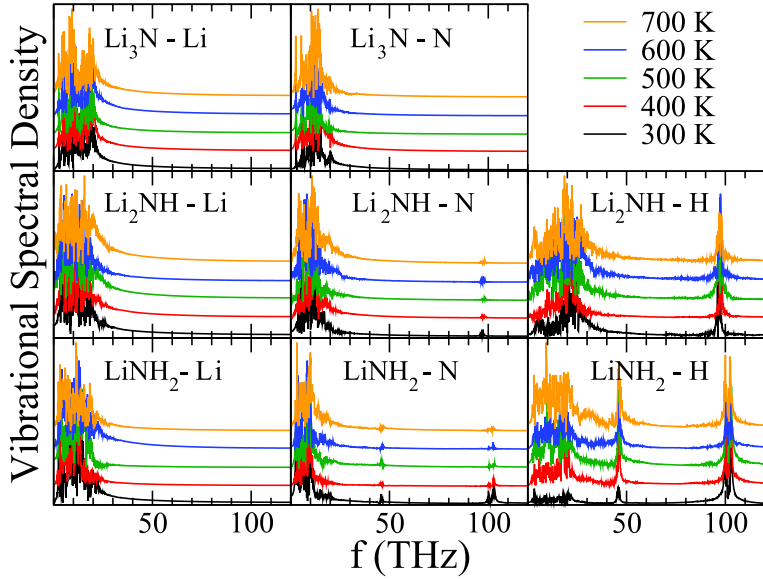


Figure 4.10: Vibrational spectral density for the different elements in  $\text{Li}_3\text{N}$ ,  $\text{Li}_2\text{NH}$ , and  $\text{LiNH}_2$ .

In  $\text{LiNH}_2$ , there is also a bending mode within the  $\text{NH}_2$ -unit which shows up at  $\sim 46$  THz.

#### 4.4.3 Diffusion barriers in $\text{Li}_3\text{N}$ , $\alpha$ and $\beta$ phase

In Paper IV we used the nudged elastic band method (NEB) [57] to find the Li diffusion barriers in  $\alpha$ - and  $\beta$ - $\text{Li}_3\text{N}$ . Commercially available  $\text{Li}_3\text{N}$  normally contains both  $\alpha$  and  $\beta$  phases of  $\text{Li}_3\text{N}$ .  $\alpha$ - $\text{Li}_3\text{N}$  is stable at room temperature and ambient pressure and belongs to the space group  $P6/mmm$  with lattice parameters of  $a=b=3.648$  Å,  $c=3.875$  Å. At a pressure of 4.2 kPa at 300 K, the loosely packed  $\alpha$ - $\text{Li}_3\text{N}$  transforms to  $\beta$ - $\text{Li}_3\text{N}$ , which belongs to the space group  $P6_3/mmc$  with  $a=b=3.552$  Å,  $c=6.311$  Å [58–61].  $\alpha$ - $\text{Li}_3\text{N}$  has been intensively studied both experimentally [62–69] and theoretically [70–74]. However, there exists no report in the literature on the  $\text{Li}^+$  ion conductivity in  $\beta$ - $\text{Li}_3\text{N}$ .

In  $\text{Li}_3\text{N}$  (either  $\alpha$  or  $\beta$ ), Li has two non-equivalent positions, denote as Li(1) and Li(2). Li(2) atoms are located in the same plane as the nitrogen atoms, forming Li(2)–N layers, which are sandwiched by pure Li(1) layers.

Figure 4.12 show the calculated migration energy profiles along the diffusion paths A1–A3 and B1–B3 (as defined in Figure 4.11). The energy barriers were estimated by the energy difference between the initial point and the saddle points of the energy profiles. For path A1 and A2, the migration energy can be determined by single step in each path as all the steps are equivalent. Our results show that the energy barrier for  $\text{Li}^+$  ion diffusion, along path A1, in the Li(2)N plane in  $\alpha$ - $\text{Li}_3\text{N}$  is 0.007 eV, which agrees

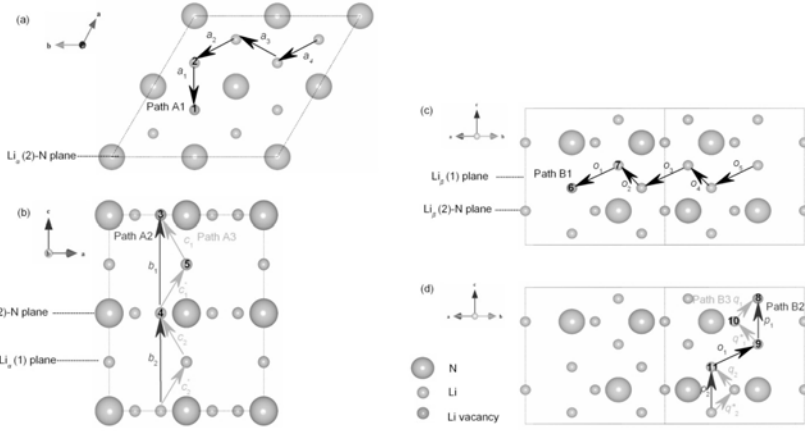


Figure 4.11: Schematic illustration of possible diffusion paths of Li ions throughout the structure to fill a vacancy. (a) path A1: Li diffusion in the  $\text{Li}_2\text{N}$  plane in  $\alpha\text{-Li}_3\text{N}$ ; (b) path A2 and path A3: interplanar Li diffusion in  $\alpha\text{-Li}_3\text{N}$ ; (c) path B1: Li diffusion within the pure Li plane in  $\beta\text{-Li}_3\text{N}$ ; (d) path B2 and path B3: inter-planar Li diffusion in  $\beta\text{-Li}_3\text{N}$ .

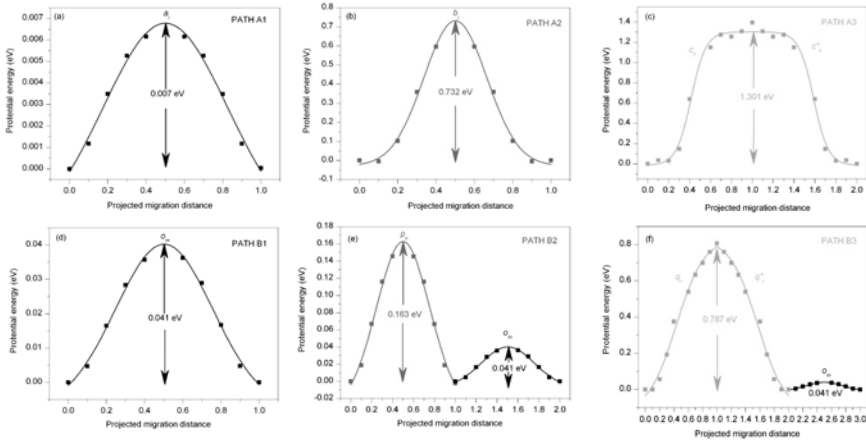


Figure 4.12: Energy profiles of Li diffusion to fill a nearest vacancy along the paths defined in Figure 4.11.

well with the J.Sarnthein's report (0.004 eV) [41]. The energy barriers of 0.732 eV and 1.301 eV for path A2 and A3, respectively, are much larger in comparison. In  $\beta$ -Li<sub>3</sub>N, the energy barrier of intra-plane diffusion along path B1 shows an estimated barrier of 0.041 eV. The diffusion along path B2 has a double barrier of 0.163 eV and 0.041 eV. The diffusion along path B3 shows an additional energy barrier of 0.787 eV. Therefore, path B1 should be the most likely diffusion path in  $\beta$ -Li<sub>3</sub>N.

Our results show that the Li<sup>+</sup> diffusion mechanism for  $\beta$ -Li<sub>3</sub>N is within the pure Li(1) plane, while for  $\alpha$ -Li<sub>3</sub>N the diffusion takes place within the Li(2)-N plane. The Li ion diffusion barriers ( $E_m$ ), with a vacancy present, for  $\alpha$  and  $\beta$  are 0.007 eV and 0.041 eV respectively. The low diffusion barriers do not allow us to use HTST to calculate the diffusion constants. Based on the big difference between the experimentally determined activation energies of 0.42 and 0.44 eV and the calculated barriers of 0.007 eV and 0.041 eV for  $\alpha$ -Li<sub>3</sub>N and  $\beta$ -Li<sub>3</sub>N, respectively, we conclude that activation energy for ionic conduction in Li<sub>3</sub>N mainly originates from formation of vacancies, in good agreement with the results from the molecular dynamics simulations in Paper III for  $\alpha$ -Li<sub>3</sub>N.



## 5. Adsorption

*God made the bulk; surfaces were invented by the devil.*

— Wolfgang Pauli

**H**IGH SURFACE AREA HYDROGEN STORAGE MATERIALS are a class of materials where hydrogen is adsorbed through physisorption on the surface. The hydrogen molecules are not split up into atomic hydrogen in the storage process, and hence the sorption kinetics is very fast. However, the van der Waals binding that holds the hydrogen molecules in the system is too weak, requiring low storage temperatures. In these systems, in contrast to storage materials where the hydrogen is chemically bonded, the binding energy has to be increased in order to be able to rise the storage temperature. In this chapter, we will discuss the nature of the hydrogen binding in metal organic frameworks (MOF) and covalent organic frameworks (COF), and how it can be improved.

The metal–organic frameworks form a class of nanoporous materials with high surface area, which are capable of binding gas molecules in a non-dissociative manner [55, 75–78]. Due to this feature, MOFs are promising candidates for application as hydrogen storage media. In these systems, the hydrogen sorption processes display good reversibility and fast kinetics. However, the weak dispersive interactions that hold H<sub>2</sub> molecules require low operation temperatures and/or high pressures in order to guarantee a significant storage capacity, e.g. MOF–5 reaches a H<sub>2</sub>–uptake of only 1.3 wt% at 78 K and 1 bar [79]. Neither the thermodynamics nor the storage capacity meet the requirements that have been set up for on-board applications [3]. Therefore, a great deal of effort is being put into devising ways of strengthening the hydrogen adsorption interactions and of maximizing the volumetric and gravimetric surface area densities. The achievement of the latter is being pursued through the following approaches: topological engineering of the pore shape [80], the insertion of other adsorbate surfaces inside the pores [81], the synthesis of light-metal MOFs [82, 83], and the entanglement of frameworks (framework catenation) [84, 85]. In order to achieve stronger H<sub>2</sub>–surface interactions, which is the more challenging problem, most of the studies have turned to investigate the introduction of electron-donating ligands to the organic linkers and also to the synthesis of so-called open metal sites [86]. In fact, it is well accepted that to significantly enhance the H<sub>2</sub> affinity in these frameworks, the binding mechanism should

include other contributions such as electrostatic and/or orbital interactions rather than being purely dispersive like [87].

High surface area hydrogen storage materials generally have very good hydrogen sorption kinetics and cyclability. Moreover, since there is no bond reconstruction in the (de-)hydrogenation process, they do not have any unwanted byproducts, which is the case for some of the chemical hydrides.

The negative side, however, of the non-dissociative bonding is the thermodynamics. Hydrogen molecules bound to a surface with van der Waals bonds typically have a binding energy of around 5 kJ/mol H<sub>2</sub>. The entropy of a hydrogen gas at room temperature is around 40 kJ/mol H<sub>2</sub> (0.41 eV/H<sub>2</sub>). In order to keep the hydrogen bound at room temperature we would need to increase the bond strength with 35 kJ/mol H<sub>2</sub>.

Two possibilities to increase the adsorption strength, without dissociating the molecule, is to either introduce electrostatic attraction or orbital interactions.

## 5.1 Strengthening the H<sub>2</sub> adsorption in MOF-5

In Paper V we investigate the possibility of introducing electrostatic attraction between MOF-5 and hydrogen molecules by decorating the framework with lithium atoms. Alkali metal ions (*e.g.* Li<sup>+</sup> and Na<sup>+</sup>) bind H<sub>2</sub> through electrostatic charge-quadrupole and charge-induced dipole interactions [87, 88]. This approach has been shown with alkali metals adsorbed on C<sub>60</sub> [89] and carbon nanotubes [90, 91]. However, in these systems the electron affinity of the host structure was not large enough, resulting in a lowering of the charge state, *e.g.* a C<sub>60</sub> molecule can accept 6 electrons while coated with 12 Li atoms, resulting in a charge state of only +1/2 on the Li.

Our approach is to let Li atoms be adsorbed on the organic linkers of MOFs. We have in particular studied the adsorption of Li on the 1,4-benzenedicarboxylate (BDC) linker in MOF-5. Metal-organic framework-5 is made up from BDC linkers joining together Zn<sub>4</sub>O clusters to form a cubic periodic framework, as shown in Figure 5.1A, which has the formula unit (f.u.) Zn<sub>4</sub>O(BDC)<sub>3</sub>. We show that two Li atoms are strongly adsorbed on the surfaces of the BDC 6-carbon rings, one on each side, carrying a charge of +0.9*e*/Li. Each Li is found to be able to cluster three H<sub>2</sub> molecules around itself with a binding energy of 12 kJ (mol H<sub>2</sub>)<sup>-1</sup>, which is more than two times larger than H<sub>2</sub> adsorption on pure BDC with a binding energy of about 5 kJ (mol H<sub>2</sub>)<sup>-1</sup> [92].

The adsorption of Li atoms on the BDC (forming BDC-Li complexes) was investigated by fully optimizing the structures with Li atoms initially placed close to the centre of the 6-atom carbon ring (C<sub>6</sub>H<sub>4</sub> units). A Bader analysis [93] of the self-consistent charge density revealed that Li atoms carry a charge of +0.9*e*/Li. Thus, the difference in the electronegativity between Li and BDC is large enough to produce the desired ionic state of Li atoms, which is beneficial to raise the H<sub>2</sub> binding affinity.

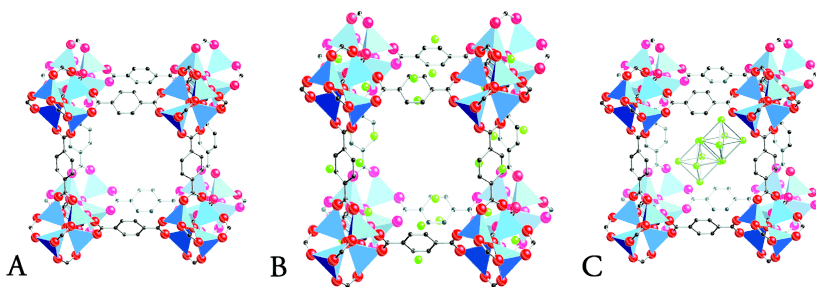


*Figure 5.1:* Metal–organic framework–5 is made up from 1,4–benzenedicarboxylate molecules joining together  $\text{Zn}_4\text{O}$  clusters forming a cubic periodic porous framework. (A) Pure MOF–5 (B) Li–decorated MOF–5 (C) MOF–5 with Li–cluster. Colour scheme as follows: C (black), Zn (blue tetrahedra), O (red), and Li (green). All H atoms have been omitted for clarity.

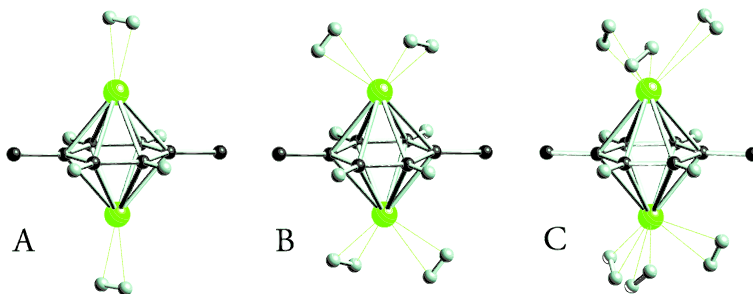


*Figure 5.2:* Optimized geometries of adsorbed hydrogen molecules on BDC:2Li in the framework of MOF–5 with (A) 1  $\text{H}_2$  per Li, (B) 2  $\text{H}_2$  per Li, and (C) 3  $\text{H}_2$  per Li. Colour scheme as follows: C (black), Li (Green), and H (Grey). The rest of the framework have been omitted for clarity.

To estimate the strength of BDC–Li interaction, we have also compared the total energy of two possible competitive configurations, namely Li adsorbed on BDC (see Figure 5.1B) and Li forming a cluster ( $\text{Li}_{12}$ ) inside the pores (see Figure 5.1C). The calculated difference of  $-0.25 \text{ eV/Li}$  shows that Li adsorbed on the BDC rings is the more stable configuration.

To investigate the hydrogen uptake, we have optimized structures with  $\text{H}_2$  molecules placed in the vicinity of the Li atoms. In Figure 5.2A–C, we display the optimized geometries as the hydrogen uptake increases from two to six molecules around the BDC:2Li complexes. We have found binding energies of  $18 \text{ kJ (mol H}_2\text{)}^{-1}$  for 1  $\text{H}_2/\text{Li}$ ,  $16 \text{ kJ (mol H}_2\text{)}^{-1}$  for 2  $\text{H}_2/\text{Li}$ , and  $12 \text{ kJ (mol H}_2\text{)}^{-1}$  for 3  $\text{H}_2/\text{Li}$ . Analyzing the charge states showed that both  $\text{H}_2$  and Li maintain their original charge state. The decrease in the binding energies as a function of cluster size is a consequence of repulsive  $\text{H}_2\text{--H}_2$  interaction.

To investigate the temperature effect on the hydrogen uptake in Li–decorated MOF–5, we have performed AIMD with two concentrations, 5 and

18 H<sub>2</sub> molecules per f.u., at the following temperatures: 20 K, 50 K, 100 K, 200 K, and 300 K.

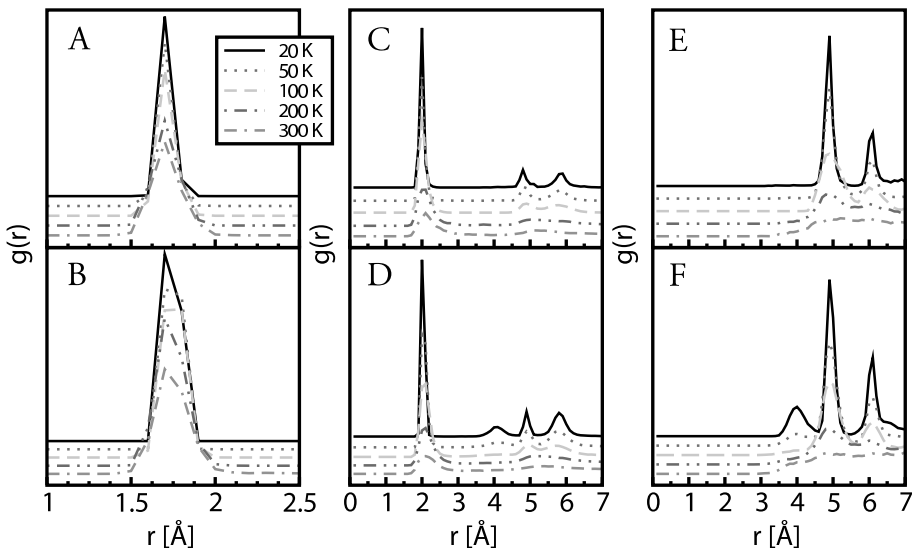


Figure 5.3: Radial distribution functions from *ab initio* molecular dynamics simulations. RDF of C<sub>6</sub><sup>CoM</sup>-Li pairs with (A) 5 H<sub>2</sub> per formula unit and (B) 18 H<sub>2</sub> per formula unit. RDF of Li-H<sub>2</sub><sup>CoM</sup> pairs with (C) 5 H<sub>2</sub> per formula unit and (D) 18 H<sub>2</sub> per formula unit. RDF of Zn-H<sub>2</sub><sup>CoM</sup> pairs with (E) 5 H<sub>2</sub> per formula unit and (F) 18 H<sub>2</sub> per formula unit.

To assess the capability of Li ions to stay attached to the BDC unit, we have calculated the RDF for C<sub>6</sub><sup>CoM</sup>-Li, where C<sub>6</sub><sup>CoM</sup> is the centre of mass of the 6-atom carbon ring. For the entire temperature range, as seen from Figure 5.3A-B, the Li stay bound to the BDC units. To investigate the population of H<sub>2</sub> adsorption, we have calculated (Figure 5.3C-F) the RDF for Zn-H<sub>2</sub><sup>CoM</sup> and Li-H<sub>2</sub><sup>CoM</sup>, where H<sub>2</sub><sup>CoM</sup> is the centre of mass of the H<sub>2</sub> molecule. An integration of the RDF shows that 2.9 wt% H<sub>2</sub> at 200 K and 2.0 wt% H<sub>2</sub> at 300 K is bound to the Li ions. This is an uptake below the saturation level, 4.3 wt%, found from 0 K calculations.

The increased binding energy of 12–18 kJ (mol H<sub>2</sub>)<sup>-1</sup> is an improvement over the 5 kJ (mol H<sub>2</sub>)<sup>-1</sup> of an undecorated BDC-linker, but still not strong enough to get the desired adsorption at room temperature.

## 5.2 The effect of metal oxide cluster

In Paper VI we have investigated the effect of the choice of metal in the metal oxide cluster of MOF-5 on the hydrogen adsorption energies. From various experimental [55, 94] and theoretical [95] investigations of MOF-5, the H<sub>2</sub> binding sites are known to be mainly located at the metal oxide clusters.

These metal oxide clusters contain the so-called "cup sites" and secondary sites; the latter can be distinguished between " $\text{ZnO}_3$ " and " $\text{ZnO}_2$ " sites and are illustrated in Figure 5.4. At higher pressures and/or very low temperatures,  $\text{H}_2$  molecules can also become adsorbed on the organic linkers [96].

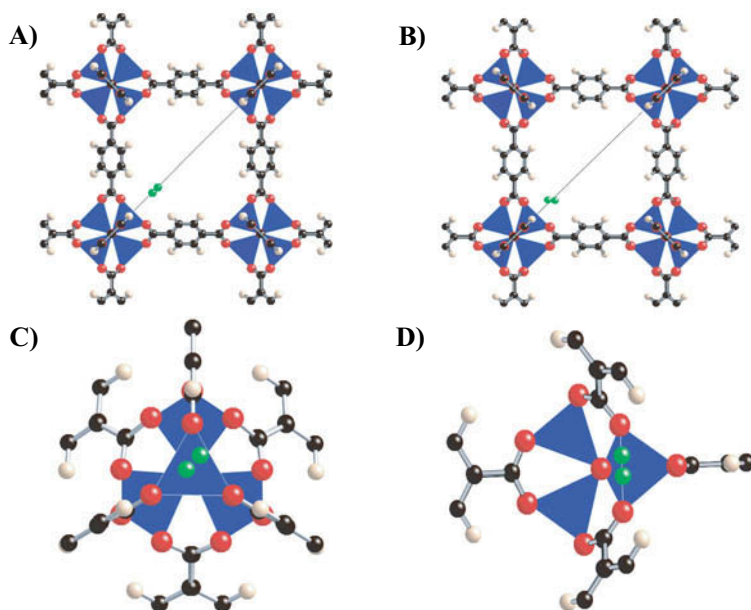


*Figure 5.4:* The  $\text{H}_2$  adsorption sites in MOF-5. Cup site: (A) adsorbed hydrogen orientation parallel to three-fold rotation axis (bold diagonal line). (B) adsorbed hydrogen orientation perpendicular to three-fold rotation axis. (C)  $\text{ZnO}_3$  site with adsorbed hydrogen. (D)  $\text{ZnO}_2$  site with adsorbed  $\text{H}_2$  molecule. The atoms are symbolized as follows: Zn (blue tetrahedra), O (red), C (black), H (white), and adsorbed  $\text{H}_2$  molecule (green).

Here, we have studied the binding energy of  $\text{H}_2$  in both Zn- and Cd-based MOF-5 using three different exchange-correlation functionals, namely, LDA [97], PW91 [11], PBE [12]. Due to the Zn-based MOF-5 system having been studied extensively [55, 80, 92, 94, 95, 98], we were able to use this system as a reference to compare our results with and to judge the suitability of the respective functionals based on their agreement with the experimental trend. Having identified the most suitable functional, we could then apply this functional to the study of Cd-based MOF-5, a system which has not yet been studied extensively. The similar electronic structures of Cd and Zn, with a 4d valence state in Cd instead of the 3d in Zn, make Cd a natural choice to replace Zn while keeping the same MOF-5 crystal structure. The common oxidation state is 2+ for both Cd and Zn, and the Pauling electronegativity is extremely similar (1.65 for Zn and 1.69 for Cd), thus requiring very little adaptation by the surrounding environment when compared to the situation in Zn-based MOF-5. The only important difference is in the ionic radius: in

EXC-func.	site	$\Delta E_b$ (meV)		
		Zn-MOF	Cd-MOF	Zn-MOF
LDA	cup	125.6	133.3	133 <sup>a</sup>
	cup $\perp$	157.7	160.4	160 <sup>a</sup>
	MO <sub>2</sub>	84.8	97.4	56 <sup>a</sup>
	MO <sub>2</sub> $\perp$	86.5	125.2	108 <sup>a</sup>
	MO <sub>3</sub>	90.2	80.8	86 <sup>a</sup>
	MO <sub>3</sub> $\perp$	110.2	149.7	115 <sup>a</sup>
GGA (PW91)	cup	18.9	22.3	—
	cup $\perp$	32.8	37.0	—
	MO <sub>2</sub>	32.7	29.2	—
	MO <sub>2</sub> $\perp$	23.2	26.4	—
	MO <sub>3</sub>	42.3	42.8	—
	MO <sub>3</sub> $\perp$	21.0	31.8	—
GGA (PBE)	cup	8.4	7.2	9.5 <sup>b</sup>
	cup $\perp$	17.3	21.3	17.9 <sup>b</sup>
	MO <sub>2</sub>	15.8	15.0	20.8 <sup>b</sup>
	MO <sub>2</sub> $\perp$	8.3	9.6	7.5 <sup>b</sup>
	MO <sub>3</sub>	22.4	16.4	20.2 <sup>b</sup>
	MO <sub>3</sub> $\perp$	13.6	17.9	12.5 <sup>b</sup>

<sup>a</sup> Ref. [94]

<sup>b</sup> Ref. [95]

Table 5.1: Binding energies of  $H_2$  in Zn-MOF and Cd-MOF at various adsorption sites, as defined in Figure 5.4, with perpendicular ( $\perp$ ) and parallel ( $\parallel$ ) orientations for three different exchange-correlation functionals, and comparison with results available in literature.

a four-coordinated environment, Zn(II) possesses an ionic radius of 74 pm, while for Cd(II) it is 92 pm. This increase in size can be easily accommodated by the porous network in MOF-5 via a simple expansion of the lattice through an "outward movement" of the organic linkers.

To calculate the hydrogen adsorption energies, we added one hydrogen molecule at the cup,  $MO_2$ , and  $MO_3$  ( $M=Zn, Cd$ ) sites and considered two different orientations of the hydrogen molecule at each site.

All adsorption sites are displayed schematically in Figure 5.4 and the corresponding binding energies are provided in Table 5.1.

According to neutron powder diffraction results on the Zn-MOF system [94], the primary adsorption site at the metal oxide cluster or cup site is the most energetically stable. The secondary adsorption sites,  $ZnO_3$  and  $ZnO_2$  sites, will start to adsorb  $H_2$  when the primary site is fully occupied. In addition, Yildirim and Hartman also reported [94] that the  $ZnO_3$  site is more stable than the  $ZnO_2$  site by considering the hydrogen binding energy. Upon comparison with our results in Table 5.1, one sees that the LDA functional leads to the best agreement with the experimental data. Therefore, LDA emerges as the most suitable functional among those tested here to study the interaction of hydrogen with the MOF-5 systems. It is however important to note that the good agreement between LDA and experiment concerns only the overall trend. The absolute values of binding energies obtained from LDA are clearly too large for a system in which the  $H_2$  molecules are bound via

physisorption. If this shortcoming is kept in mind, one can certainly rely on LDA as a very useful tool in the theoretical estimation of binding energy trends even in physisorbed systems.

Overall, our results show that the binding energy is very much affected by the choice of functional for both Zn–MOF and Cd–MOF. Based on our LDA results shown in Table 5.1, the adsorption energies for Zn–MOF and Cd–MOF are found to be almost equal at the primary adsorption site, but the hydrogen binding energy for Cd–MOF at the secondary adsorption site is increased by about 25% at both the  $MO_3$  and  $MO_2$  sites, compared to Zn–MOF. The increase in the binding energy at the secondary sites is due to the larger size of Cd compared to Zn. The increase in size leads to a more open structure, allowing an  $H_2$  molecule to approach closer and thus interact more strongly.

### 5.3 Alkali decorated (Zn–/Mg–/Ca–)IRMOF–16

In Paper VII we consider the effect of decorating with either Li, Na, or K, in three different types of iso–reticular Metal Organic Framework–16, Zn–/Mg–/Ca–IRMOF–16. The difference between MOF–5 and IRMOF–16 is the length of the organic linker (see Figure 5.5), resulting in more adsorption sites.

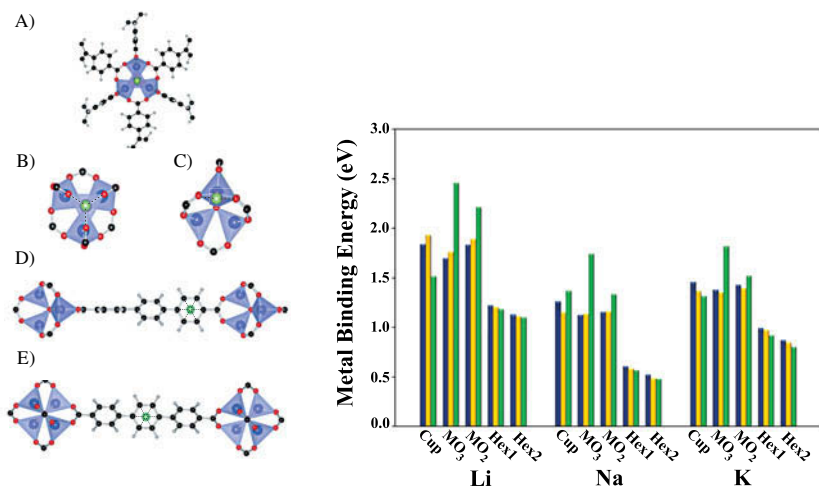


Figure 5.5: In the left panel, the metal binding sites in  $M$ –IRMOF–16 ( $M = \text{Zn, Mg, Ca}$ ) are shown. (A) Cup site which is an adsorption site on the centre of three  $MO_4$  tetrahedra. (B)  $MO_3$  site. (C)  $MO_2$  site. (D) Hex1 site. (E) Hex2 site. Colours:  $M$  (blue tetrahedra), O (red), C (black), H (white), alkali metal (green). The corresponding alkali metal binding energies ( $\Delta E_M$ ) are shown in the right panel for Zn–IRMOF–16 (blue), Mg–IRMOF–16 (yellow), and Ca–IRMOF–16 (green).

The different metal binding sites studied are displayed in the left panel of Figure 5.5. In the right panel of Figure 5.5, the binding energies are displayed. As can be seen, metal binding energies of alkali metals at the adsorption sites close to the metal oxide cluster are always higher than those at the sites on the

organic linker. The alkali metals (positive charge) bind strongly to the oxygen atoms (negative charge), whereas the interaction energy at the organic linker arises from the combination of chemical bond due to overlapping of atomic orbital between alkali metal states and host framework states and electrostatic interaction between charged alkali metals and induced charge on the benzene ring where the metal is trapped.

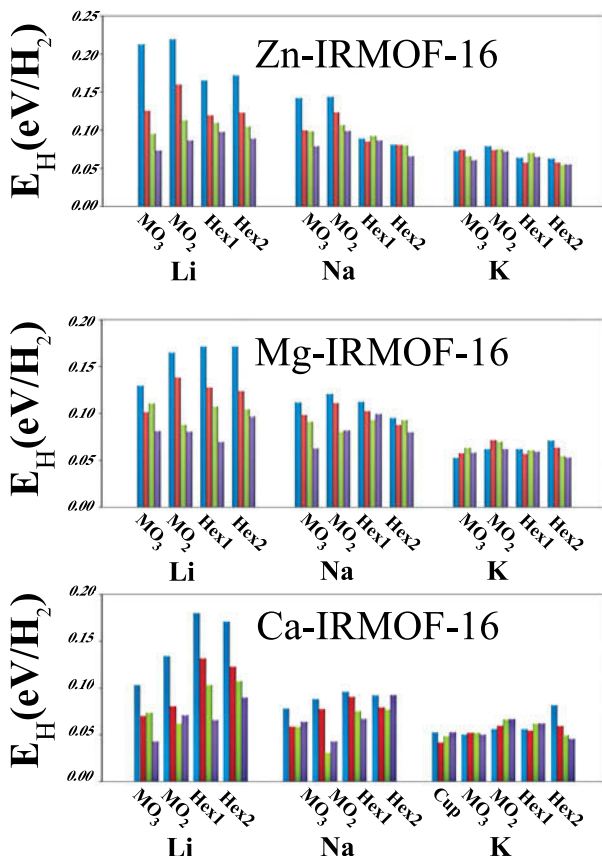


Figure 5.6: Hydrogen interaction energies ( $\Delta E_{H_2}$ ) at different levels of hydrogen loading ( $n = 1-4$  H<sub>2</sub>) of Li, Na, and K trapped at all studied adsorption sites in Zn-, Mg-, and Ca-IRMOF-16. The colours label the different degrees of hydrogen loading: 1 H<sub>2</sub> (blue), 2 H<sub>2</sub> (red), 3 H<sub>2</sub> (green), and 4 H<sub>2</sub> (purple). Except for K-decorated Ca-IRMOF-16, alkali metals exhibited large deviations from the ideal position of cup site and therefore the corresponding binding energies are omitted here.

To determine the hydrogen adsorption energy, different levels of hydrogen loadings, namely 1–4 H<sub>2</sub>, were inserted on top of an alkali metal trapped at a given adsorption site. In order to maximize charge–quadrupole interaction, only the side–on configuration of hydrogen molecules relative to the alkali metal is considered as an initial configuration for geometry relaxations [99]. The hydrogen interaction energies from one to four H<sub>2</sub> loadings placed on the

alkali metal decoration in three types of  $M$ -IRMOF-16 ( $M = \text{Zn}$ ,  $\text{Mg}$ , and  $\text{Ca}$ ) are displayed in Figure 5.6.

Concerning the binding strengths of the alkali metals, our density functional theory calculations reveal that Li is strongest bound in the host framework, followed by K and Na. Decoration with Li also results in the highest hydrogen adsorption energies among the studied alkali metals. Furthermore, Zn-IRMOF-16 exhibits the highest hydrogen adsorption energies near the metal oxide cluster, while hydrogen binding strengths at organic linker sites do not differ substantially between Zn-/Mg-/Ca-IRMOF-16. Based on our results, we conclude that for Metal Organic Framework-16, Li-decorated Zn-IRMOF-16 appears to be the best choice for hydrogen storage among the nine combinations studied by us.

## 5.4 Hydrogen interaction with COF-1

In Paper VIII the interaction between  $\text{H}_2$  and Covalent Organic Framework-1 (COF-1) is investigated by density functional theory (DFT) and second-order Møller-Plesset perturbation theory (MP2). The structure of COF-1 is displayed in Figure 5.7.

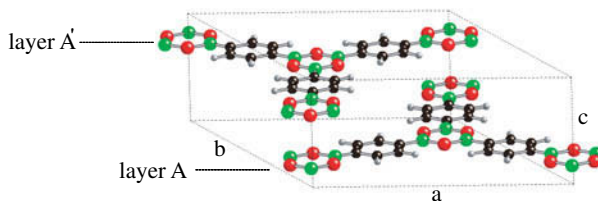
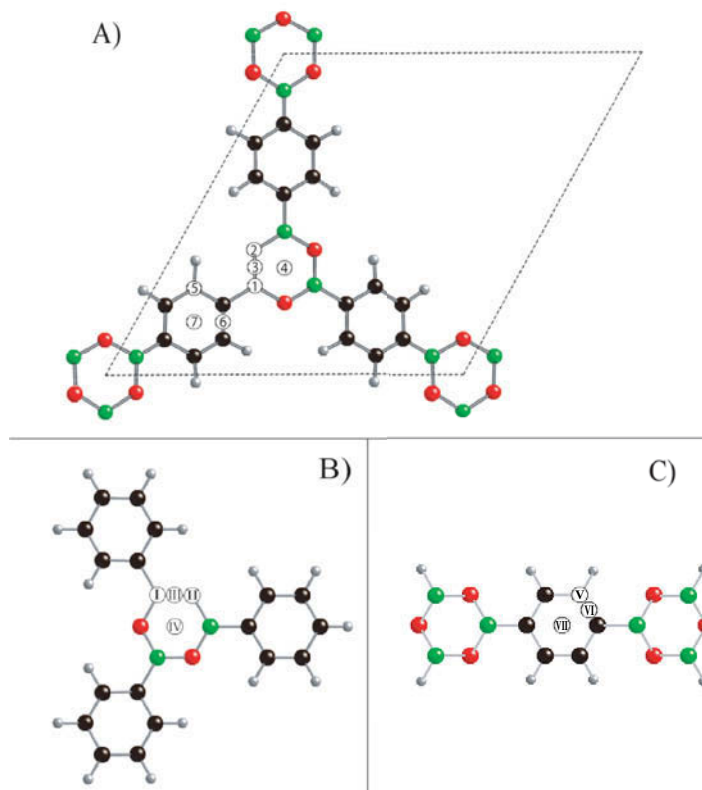


Figure 5.7: The COF-1 unit cell. Green, red, black and grey spheres represent B, O, C and H atoms, respectively. Some atoms that lie outside the unit cell have been included to facilitate a better viewing of the structure.

To calculate the binding strength of an interaction which is mainly mediated through van der Waals bonds, electron correlation is important. Electron correlation effects are included in MP2, in contrast to standard DFT. The downside of using MP2 however, is that the computational cost is much higher. Therefore we have chosen an approach where we combine the two methods. MP2 calculations are used to calculate the interaction between  $\text{H}_2$  and a cluster cut out from the system, while DFT is used to calculate the interaction between  $\text{H}_2$  and the full periodic framework.

The adsorption sites where we calculated the interaction energy are defined in Figure 5.8A for the periodic system, and in Figure 5.8B-C for the clusters. The calculated binding energies are displayed in Figure. 5.9. As can be seen, the difference in energy between the two different methods is more than one order of magnitude. This is due to over-binding introduced by the LDA functional in the DFT calculations. If we look at the trend of the



*Figure 5.8:* (A) Hydrogen adsorption sites in COF-1. Numbers 1 through 7 correspond to the different sites as follows: 1 boron site, 2 oxygen site, 3 and 4 bridge and hollow sites of B<sub>3</sub>O<sub>3</sub> ring, respectively, 5 carbon site, and 6 and 7 bridge and hollow sites of benzene ring, respectively. (B) The roman numerals I, II, III, and IV denote the adsorption sites of the B<sub>3</sub>O<sub>3</sub> cluster for our MP2 calculations and refer to the boron site, oxygen site, bridge, and hollow sites, respectively. (C) The roman numerals V, VI, and VII indicate trapping sites of the C<sub>6</sub>H<sub>4</sub> cluster in the following order: carbon site, bridge, and hollow sites.

binding energies however, the agreement between the two methods is good. The discrepancy at site 7/VII is due to interactions from the second layer in the periodic system, which is not present in the cluster calculation.

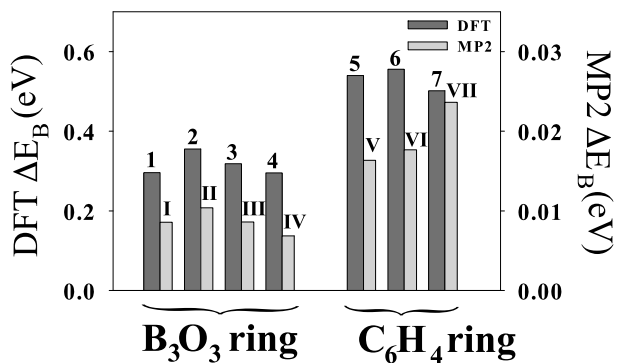


Figure 5.9: Binding energies of a single hydrogen molecule on a boron site, an oxygen site, a carbon site, on bridge and hollow sites on B<sub>3</sub>O<sub>3</sub> and C<sub>6</sub>H<sub>4</sub> rings (sites are defined in Figure 5.8). The dark red and light blue bars refer to the hydrogen adsorption energies at the above adsorption sites of B<sub>3</sub>O<sub>3</sub> and C<sub>6</sub>H<sub>4</sub> rings as calculated by DFT and MP2 methods, respectively.



## 6. Catalysts

*If I could explain it to the average person, I wouldn't have been worth the Nobel Prize.*

— Richard Feynman

IN CHEMICAL HYDRIDES the hydrogen molecules splits on the surface of the storage material and diffuses into the material, to form new chemical bonds with the host. What determines the hydrogen sorption properties of a material is the thermodynamics and the kinetics. The thermodynamics of the hydrogen sorption reaction can be investigated by first calculating the reaction enthalpy,  $\Delta H^0$ , and entropy,  $\Delta S^0$ , which can be written as,

$$\Delta H^0 = H_{M_yH_x}^0 - (H_{yM}^0 + H_{\frac{x}{2}H_2}^0) \quad (6.1)$$

and

$$\Delta S^0 = S_{M_yH_x}^0 - (S_{yM}^0 + S_{\frac{x}{2}H_2}^0), \quad (6.2)$$

where  $H_{M_yH_x}^0$  and  $S_{M_yH_x}^0$  are the enthalpy and entropy of the fully hydrogenated state,  $M_yH_x$ , and,  $H_{yM}^0 + H_{\frac{x}{2}H_2}^0$  and  $S_{yM}^0 + S_{\frac{x}{2}H_2}^0$  are the enthalpy and entropy of the dehydrogenated state,  $yM + \frac{x}{2}H_2$ . To find the transition temperature where the hydrogen desorption becomes favourable, we minimize the Gibbs free energy,  $\Delta G$ ,

$$\Delta G = \Delta H^0 - T\Delta S^0. \quad (6.3)$$

Now we have the temperature,  $T$ , where the entropy driven hydrogen desorption becomes favourable. This does however not mean that this will be the practical desorption temperature in a material. Although the desorption starts due to the thermodynamics, the kinetics will determine how fast the hydrogen desorbs. Most of the complex light metal hydrides have poor kinetics due to the strong chemical bonds with the atomic hydrogen, and therefor requires a desorption temperature which is much higher than the temperature determined by the thermodynamics.

In order to improve the kinetics of a system, different catalysts are being studied in order to be able to increase the hydrogen desorption speed. We have studied the hydrogen storage properties of alanates ( $\text{NaAlH}_4$  and  $\text{NaBH}_4$ ) by investigating the effect of transition metal impurities (Paper IX and X) and carbon nanostructures (Paper XI) acting as catalysts.

## 6.1 Hydrogen sorption catalysts, transition metals

### 6.1.1 NaAlH<sub>4</sub>

Following the pioneering work of Bogdanovic and Schwickardi [100] sodium alanate (NaAlH<sub>4</sub>) has become a hydrogen storage material of high interest. Bogdanovic and Schwickardi showed that the addition of small amounts

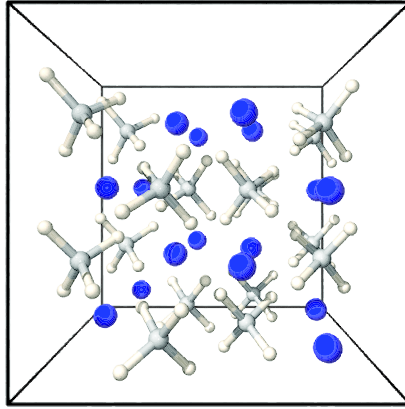
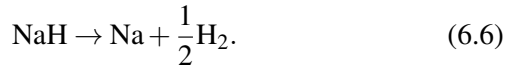
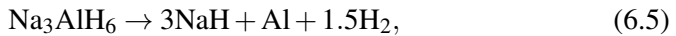
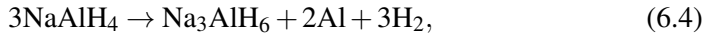


Figure 6.1: A 2x2x1 supercell of the NaAlH<sub>4</sub> crystalline structure, space group  $I4_1/a$  (#88). Na atoms shown in blue, Al in grey, and H in white.

of titanium can greatly improve the kinetics of the hydrogen desorption in sodium alanate, and more importantly also make the hydrogen desorption reversible. The hydrogen desorption in sodium alanate takes place in the following three steps,



However, the third step in the reaction takes place at high temperatures so the practical hydrogen storage capacity is calculated from what is released in the first two parts of the reaction. This yields a hydrogen storage capacity of 5.6 wt% hydrogen.

Although more than a decade has passed since Ti was identified as a good catalyst for sodium alanate, there is still an ongoing discussion on what the effect of Ti is [101–114]. Sodium alanate is made up from positively charged Na<sup>+</sup> and negative AlH<sub>4</sub><sup>−</sup> and has a  $I4_1/a$  crystal structure shown in Figure 6.1.

In order to understand the effect of the catalyst and to search for other catalysts, we have conducted a systematic study of 3d-transition metals (*TM*) as impurities in sodium alanate. The objectives of our study are to determine the energy cost to remove a hydrogen atom from the vicinity of the dopant

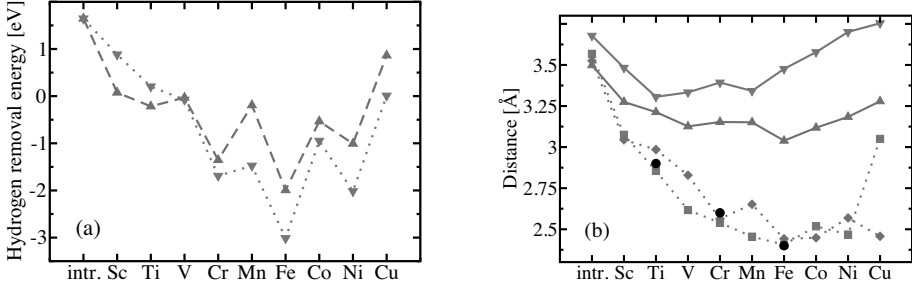


Figure 6.2: (a) Hydrogen removal energy when  $TM@Al$  (▼··▼) and  $TM@Na$  (▲---▲). (b)  $TM-Al$  distance before removal of hydrogen when  $TM@Al$  (▼··▼) and  $TM@Na$  (▲---▲);  $TM-Al$  distance after removal of hydrogen when  $TM@Al$  (■··■) and  $TM@Na$  (◆··◆); First RDF  $TM-Al$  peak from MD simulations (●). ( $TM@Na$   $\equiv$   $TM$  replacing  $Na$  site)

and the changes in the local atomic environment around the dopant before and after hydrogen is removed.

The energy cost to remove one hydrogen,

$$\Delta E_H^{TM} = E(TM_{x+y}Na_{16-x}Al_{16-y}H_{63}) - E(TM_{x+y}Na_{16-x}Al_{16-y}H_{64}) + \frac{1}{2}E(H_2), \quad (6.7)$$

is calculated as the difference in total energies of the fully hydrogenated  $2 \times 2 \times 1$  supercell and the supercell without one hydrogen atom, using molecular hydrogen as the reference chemical potential. The values of the removal energies when the 3d-transition metals substitute either Na and Al atoms are displayed in Figure 6.2a. The trend of the removal energies could not be explained just by looking at the electronic structure following the doping. What was noticed was that following the removal of hydrogen, large relaxations around the dopants occurred (see Figure 6.2b). After the removal of one hydrogen atom the 3d-transition metal dopant seemed to form bonds with the surrounding Al atoms. In fact, when we looked at the trend of the removal energies and the local relaxations, we found that these two properties were closely linked.

In order to investigate whether this was an effect of the hydrogen removal or if the relaxations were prevented by energy barriers that could not be overcome at 0 K, we decided to perform *ab initio* molecular dynamics simulations at 400 K. In Figure 6.3 the RDF of Fe-Al, Cr-Al, and Ti-Al are shown. What can be noticed is that irrespectively of whether the  $TM$  is at the Na or Al site the bond distances to Al become the same. Furthermore, while looking at Figure 6.2b, we notice that the  $TM-Al$  distances from the MD simulations coincide with the distance after the removal of hydrogen.

The ability of a transition metal dopant to promote dehydrogenation is found to be correlated to its tendency to form bonds with Al atoms supporting the most widely accepted explanation of the role of Ti on the hydrogen

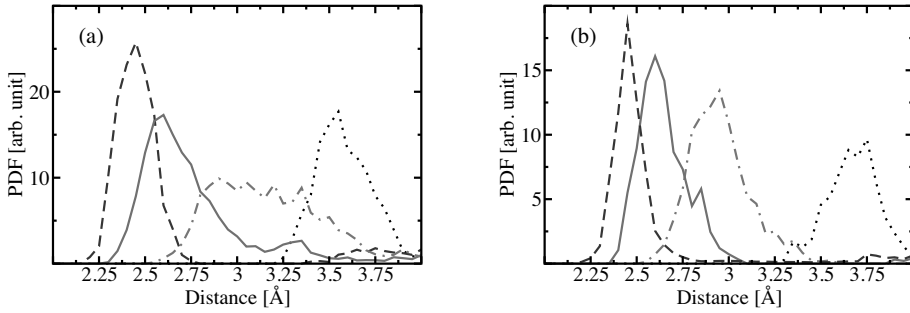
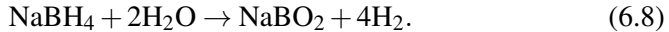


Figure 6.3: Radial distribution function from 400 K AIMD simulations. (a) Fe–Al (dashed), Cr–Al (solid) Ti–Al (dashed dotted) when  $TM@Na$  site and Na–Al (dotted) in pure  $NaAlH_4$ . (b) Fe–Al (dashed), Cr–Al (solid) Ti–Al (dashed dotted) when  $TM@Na$  site and Al–Al (dotted) in pure  $NaAlH_4$ .

sorption [104, 106, 107, 109]. In particular, we show that Cr and Fe atoms may be even more effective catalysts than Ti for hydrogen desorption.

### 6.1.2 $NaBH_4$

Sodium borate ( $NaBH_4$ ) slurry has been indicated as one of the most promising systems for applications on fuel cell technology [115–118]. This solution not only has a high storage capacity, 10.9 wt%, but also provides one of the simplest ways of generating hydrogen through the following heat-releasing reaction



This reaction is activated by adding a proper catalyst and can be operated at ambient conditions. Furthermore, the by-product  $NaBO_2$  can be recycled into  $NaBH_4$  through a fuel recovery reaction making the hydrolysis above a renewable process [116]. Additionally, the  $NaBH_4$  itself is also a promising hydrogen storage material since it has one of the highest gravimetric hydrogen densities, 10.7 wt%, among the alkali metal hydrides [3]. However, it is irreversibility with respect to the hydrogen absorption–desorption cycle and the high dissociation temperature limits the practical application for hydrogen storage. Therefore, it is worthwhile to conduct studies aimed at finding ways to overcome such limitations making  $NaBH_4$  a suitable material for on-board applications.

Following our work on sodium alanate we have tried doping sodium borate with Ti. To estimate the change in the strength of the B–H bond induced by the presence of Ti, we have evaluated the energy needed to remove a hydrogen atom from  $Na_8B_8H_{32}$  and  $(TiNa_7)B_8H_{32}$  super-cells. Therefore, we have computed the total energies of  $Na_8B_8H_{31}$  and  $(TiNa_7)B_8H_{31}$  super-cells in which one of the hydrogen atom bound to Ti and its equivalent atom bound to Na were, respectively, removed. The energies needed to remove a H

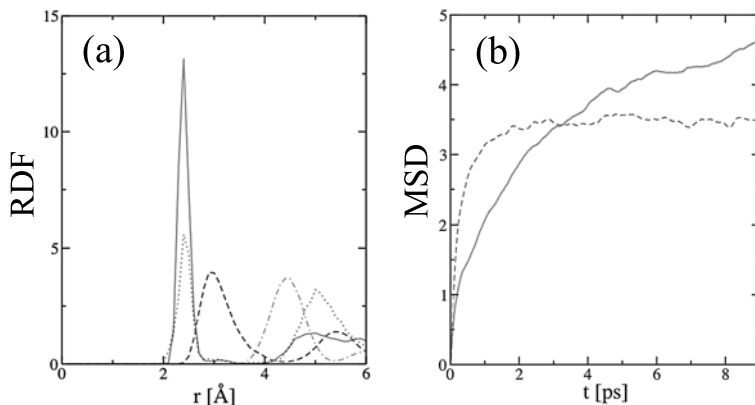


Figure 6.4: (a) Radial distribution function from 400 K AIMD. Solid and dotted lines represent Ti–B pairs when Ti substitute Na (in  $\text{TiNa}_7\text{B}_8\text{H}_{32}$  super-cell) and B (in  $\text{Na}_8\text{TiB}_7\text{H}_{32}$  super-cell), respectively. Dashed and dotted dashed lines represent the Na–B and B–B pairs in the pure  $\text{NaBH}_4$ , respectively. (b) Mean square displacement of hydrogen atoms in  $\text{Na}_8\text{TiB}_7\text{H}_{32}$  (dashed line) and  $\text{Na}_8\text{B}_8\text{H}_{32}$  (solid line) super-cells.

atom from  $\text{Na}_8\text{B}_8\text{H}_{32}$  and  $(\text{TiNa}_7)\text{B}_8\text{H}_{32}$  super-cells are 5.64 eV and 4.77 eV, respectively. This confirms that Ti doping does weaken the B–H bond.

As a second step, we decided to evaluate the distance between Ti and the nearest B atom before and after the hydrogen removal. For the former case, we found a distance of 2.8 Å, which is quite close to the Na–B distance in the intrinsic system showing that there is not much relaxation following the Ti substitution. However, as hydrogen is removed the Ti–B distance reduces to 2.3 Å.

To investigate whether the reason for Ti–B not to form bonds before the hydrogen removal is due to potential energy barriers, as was the case for *TM* in sodium alanate, we have performed *ab initio* MD simulations at 400 K. In order to analyze the bond formations, we have evaluated the RDF. In Figure 6.4a, we display the RDF for Ti–B (in  $\text{TiNa}_7\text{B}_8\text{H}_{31}$  and  $\text{Na}_8\text{TiB}_7\text{H}_{32}$ ), Na–B and B–B (in  $\text{Na}_8\text{B}_8\text{H}_{32}$ ), averaged over about 8 ps. The first Ti–B RDF peak is located at around 2.3 Å regardless which site Ti occupies. It should be highlighted that when Ti occupies a B site, the Ti–B distance changed from the initial value of 4.4 Å (the position around which the B–B peak is situated) to the value of 2.3 Å. These results strongly confirm the tendency of Ti and B to form bonds. Therefore, the introduction of Ti in  $\text{NaBH}_4$  may lead to formation of Ti–B inter-metallic phases, which may be related to the catalytic mechanism.

Actually, the latter is corroborated by the fact that in the doped system the hydrogen atoms travel more freely between Ti and B. The higher mobility of hydrogen atoms was evaluated from the MSD, shown in Figure 6.4b. The MSD for the hydrogen atoms in  $\text{Na}_8\text{TiB}_7\text{H}_{32}$  has a significantly larger inclination as compared to that of the hydrogen atoms in  $\text{Na}_8\text{B}_8\text{H}_{32}$  meaning that the hydrogen atoms are more mobile in the doped systems.

## 6.2 Hydrogen sorption catalysts, carbon nanostructures

In Paper XI, a synergistic approach involving experiment and first-principles theory not only shows that carbon nanostructures can be used as catalysts for hydrogen uptake and release in complex metal hydrides such as sodium alanate,  $\text{NaAlH}_4$ , but also provides an unambiguous understanding of how the catalysts work. To study the interaction of sodium alanate with the carbon nanostructures (fullerenes, nanotubes, and graphene), we modelled sodium alanate with a single formula unit, namely a  $\text{NaAlH}_4$  cluster.

We have considered zero-, one-, and two-dimensional carbon nanomaterials, namely  $\text{C}_{60}$ , single-walled carbon nanotubes of (5,0), (4,4), (5,5), and (8,0) type, and graphene. The  $\text{NaAlH}_4$  cluster was found to preferably bind with the Na atom facing toward the carbon substrates. Figure 6.5 shows the equilibrium geometry of the  $\text{NaAlH}_4$  cluster supported on the (5,0) carbon nanotube (CNT),  $\text{C}_{60}$  fullerene, and graphene.

The binding energies, and the interaction, of the  $\text{NaAlH}_4$  cluster to these structures were weak ( $<0.1$  eV). On the other hand, the substrates have a dramatic effect on the hydrogen removal energy. These are calculated using the equation

$$\Delta E = E(\text{CS}/\text{NaAlH}_3) + E(\text{H}) - E(\text{CS}/\text{NaAlH}_4), \quad (6.9)$$

Here CS stands for a given carbon substrate (nanotube, fullerene, or graphene). The calculations of the removal energies require optimizing the geometry of  $\text{NaAlH}_3$  interacting with various nanostructures. The results are given in Figure 6.5. Note that it costs 3.8 eV to remove a H atom from an isolated  $\text{NaAlH}_4$  cluster while it costs only 2.0 eV to remove the H atom when the  $\text{NaAlH}_4$  cluster is supported on a (5,0) CNT. This is nearly the same energy as when Ti replaces the Na atom in a  $\text{NaAlH}_4$  crystal. [113, 114] We also note from Figure 6.5 that the hydrogen removal energy from  $\text{NaAlH}_4$  supported on graphene is high, namely 3.60 eV, and that it varies between 2.95 to 3.07 eV in (4,4), (5,5), and (8,0) nanotubes. For the  $\text{C}_{60}$  fullerene, the hydrogen removal energy is about 2.85 eV.

We have calculated the electron affinities of the carbon nanostructures to determine the origin of and energy difference for the hydrogen removal from supported  $\text{NaAlH}_4$ . The electron affinity is found to depend upon the curvature of the substrate and increases with increasing curvature. In addition, as the electron affinity of the substrate decreases, the energy to remove the hydrogen atom increases.

The stability of the  $\text{NaAlH}_4$  cluster is governed by the charge transfer from Na to  $\text{AlH}_4$ , transforming the former into a cation and the latter into an anion. Thus, the way to reduce the bond strength between Al and H in  $\text{NaAlH}_4$  would be to introduce a competitor for the charge donation from the Na atom. This can be provided through a substrate with a high electronegativity, competing with  $\text{AlH}_4$  to obtain the electron from Na, which would result in a lowering of the of the hydrogen desorption energy.

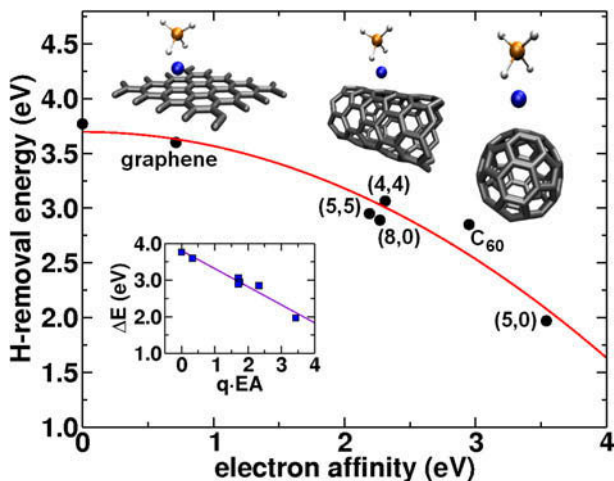


Figure 6.5: Correlation of the carbon substrate electron affinity and the hydrogen removal energy. Black circles are *ab initio* results for H-removal energy as a function of electron affinity (EA) of the carbon substrate. The red curve is a fit of the data with a quadratic function. The inset below the red curve shows the linear relationship between the H-removal energy ( $\Delta E$ ) to the product of transferred charge,  $q$ , and EA. The inset above the red curve displays the equilibrium configurations for NaAlH<sub>4</sub> interacting with a graphene sheet, (5,0) zigzag carbon nanotube, and fullerene. Na atoms are shown as blue spheres, Al in gold, C in dark gray, and H in white.

The plot of the electron affinity of the carbon nanostructures versus the hydrogen removal energy is best fitted by a parabola. Note that the hydrogen removal energy decreases as the electron affinity of the substrate increases. This relationship may be understood as follows. Once the hydrogen atom has left the NaAlH<sub>4</sub> cluster, the remaining NaAlH<sub>3</sub> unit can transfer charge to the carbon support and thus bring the total energy of the system to a lower level. The amount by which the energy can be lowered depends on two factors: (i) the electron affinity of the charge-receiving carbon nanomaterial, and (ii) the amount of charge actually being transferred from the NaAlH<sub>3</sub> molecule. The latter is determined by the cost of energy to remove a charge,  $q$ , from NaAlH<sub>3</sub> and the gain in energy due to the carbon nanomaterial accepting this charge. The difference between these two energy terms corresponds to the amount by which the system can actually lower its total energy. Hence, the  $q$  for which this difference reaches its maximum is the charge that will be transferred. This resulting energy gain is, to a good approximation, proportional to the product of charge and electron affinity as long as the transferred charge amount is comparatively small ( $q < 1e$ ). As the amount by which the final state lowers its energy directly affects the hydrogen removal energy, we find that the decrease of the latter is indeed proportional to the product of transferred charge and electron affinity (inset of Figure 6.5).



## 7. Structure

*One of the continuing scandals in the physical sciences is that it remains impossible to predict the structure of even the simplest crystalline solids from a knowledge of their composition.*

— John Maddox

NEXT TO THE COMPOSITION, the structure of a material determines its properties. Therefore, it is essential to know the structure in order to understand the properties of a material. Predicting crystal structures has been a long standing challenge in condensed matter science [119]. Different methods, *e.g.* simulated annealing, generic algorithms, or random search, have been developed to predict crystal structures.

### 7.1 *Ab initio* random search

To search the configurational space, we have used an *ab initio* random search (AIRS) method, similar to the method successfully employed by Pickard and Needs [120–122]. In order to lower the computational cost, we have used a structure generation scheme which considers space group symmetries. This results in an efficiency gain which is estimated to one order of magnitude, due to the smaller size of the irreducible Brillouin zone. The procedure to create a structure is:

- 1 a random space group is selected.
- 2 the length of the lattice vectors are randomized, keeping a reasonable volume to get a specific pressure.
- 3 a set of sub-groups, and coordinates, are selected randomly to match the stoichiometry of the material.
- 4 a k-point grid is generated with a homogeneous density of k-points in each direction.
- 5 the structure is allowed to relax.

After this is repeated a few thousand times, the enthalpies of the relaxed structures are compared.

### 7.1.1 AIRS for BeC<sub>2</sub> structure

In Paper XII, we employ the space group enhanced AIRS formalism to search the configurational space of BeC<sub>2</sub>. In nanotechnology, low-dimensional carbonaceous nanostructures such as graphene, nanotubes, nanoribbons, fullerenes, nanowires, etc., show promising results [123–131]. For metal dicarbide systems, many studies exist in the literature, *e.g.*, on second-row dicarbides (XC<sub>2</sub>, X=Na–Cl) [132–134], transition metal dicarbides [135], rare earth dicarbides [136], and also on alkaline earth dicarbides [137–143]. Most alkaline earth dicarbide systems were found to have a linear-type crystal structure [137, 138]. According to experimental results, magnesium dicarbide (MgC<sub>2</sub>) crystal structure at room temperature has a tetragonal unit cell (space group  $P4_2/mnm$ ), with C<sub>2</sub> dumbbells which are aligned in the perpendicular direction of the tetragonal *c*-axis [139]. For the CaC<sub>2</sub> crystal structure, both experimental and theoretical studies agree on the  $I4/mmm$  space group [140, 141]. The only difference in crystal structure between MgC<sub>2</sub> and CaC<sub>2</sub> is the direction of the C<sub>2</sub> alignment, namely parallel orientation of the C<sub>2</sub> dumbbells to the tetragonal *c*-axis for CaC<sub>2</sub> and perpendicular orientation for MgC<sub>2</sub>. X-ray diffraction experiments revealed that the crystal structures of SrC<sub>2</sub> [142] and BaC<sub>2</sub> [143] at room temperature are analogous to that of CaC<sub>2</sub>.

For BeC<sub>2</sub>, Zaleski-Ejgierd *et al.* [144] performed first-principles calculations on both a sheet-type and a chain-type structure, showing that the total energy of the sheet-type structure is lower than that of the chain-type structure which was found experimentally for the other alkaline earth dicarbides. However, the vibrational spectrum at the centre of the Brillouin zone ( $\Gamma$ -point) of the lowest energy sheet structure showed large imaginary frequencies, indicating a dynamical instability.

From an *ab initio* random structure search for the ground state crystal structure of BeC<sub>2</sub>, we found that the lowest energy configuration, shown in Figure 7.1, of BeC<sub>2</sub> resembles a poly[hexadehydro(methyl-cyclopentadiene)] (abbreviated as PH-MCP)-like carbon chain surrounded by Be ions. This new BeC<sub>2</sub> structure is 1.2 eV/f.u. more stable as compared to the sheet structure. Applying the same configuration to the MgC<sub>2</sub> system, our results reveal that the total energy of this new crystal structure is actually lower than the chain-type crystal structure of MgC<sub>2</sub> reported from experiments by 0.2 eV/f.u. The lowest energy configuration of MgC<sub>2</sub> is thus analogous to BeC<sub>2</sub>, *i.e.*, the PH-MCP-like anionic carbon surrounded by Mg ions, whereas chain-type crystal structures reported from experiments are more stable than the PH-MCP-like crystal structure for CaC<sub>2</sub>, SrC<sub>2</sub>, and BaC<sub>2</sub>.

## 7.2 Alloy of incompatible elements

In Paper XIII, the synthesis of a non-Hume-Rothery random alloy is demonstrated and explained. The formation of substitutional alloys has been

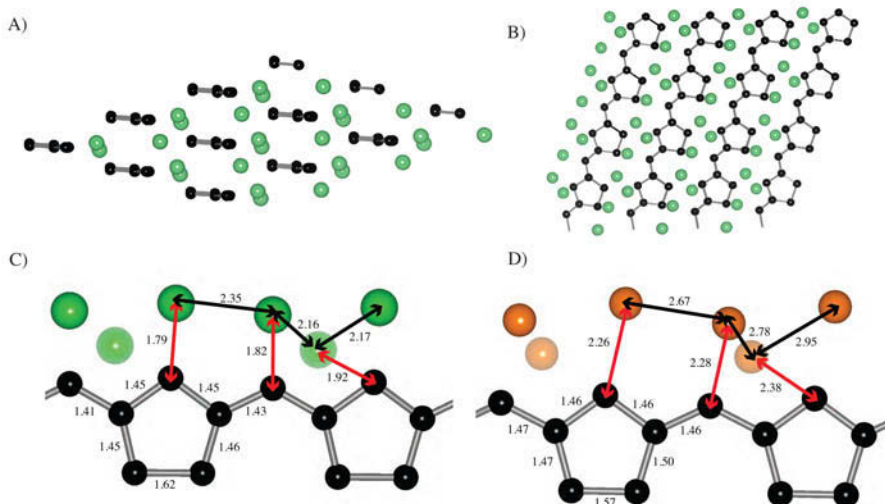


*Figure 7.1:* Lowest energy configurations for  $\text{BeC}_2$  and  $\text{MgC}_2$ . The structure resembles a PH-MCP anionic chain surrounded by alkaline earth metals. (A) Side view. (B) Top view. Purple spheres refer to alkaline earth metals (either Be or Mg) and black spheres represent C atoms. Structural parameters are shown in (C) for  $\text{BeC}_2$  and in (D) for  $\text{MgC}_2$ . The numbers indicate the bond lengths or distances between pairs of atoms in units of Å. Green spheres in (C) represent Be atoms, while orange spheres in (D) represent Mg atoms. C atoms are again drawn in black.

restricted to elements with similar atomic radii and electronegativity. The empirical Hume-Rothery (HR) rules [145] state that the constituents of a solid solution may not have a difference in radii larger than 15%, or a difference in electronegativity larger than 0.4 (Pauling scale).

No known binary substitutional crystalline alloy exists between Ce and Al because their differences of 28% in atomic radii and 0.45 in electronegativity far exceed the HR limits. They can only form stoichiometric compounds in which Ce and Al are chemically ordered and occupy separate crystallographic sites, or as metallic glass synthesized from rapidly quenched melt in which Ce and Al are disordered both chemically and structurally.

Using high-pressure at 298 K, we synthesized a *fcc* disordered alloy of highly dissimilar elements (large Ce and small Al atoms) by compressing a  $\text{Ce}_3\text{Al}$  intermetallic compound >15 GPa and a  $\text{Ce}_3\text{Al}$  metallic glass >25 GPa. Measurements with synchrotron X-ray diffraction, Ce  $L_3$ -edge absorption spectroscopy, and *ab initio* calculations revealed that a pressure-induced volume collapse and  $4f$  electron delocalization of Ce reduced the differences between Ce and Al and brought them within the Hume-Rothery limits for substitutional alloying. The alloy remained after release of pressure, which was also accompanied by the transformation of Ce back to its ambient  $4f$  electron localized state and reversal of the volume collapse, resulting in a non-HR alloy at ambient conditions.

The surprising discovery of the *fcc*-Ce<sub>3</sub>Al substitutional alloy may be understood by considering the effect of pressure on Ce. We conducted *ab initio* calculations for the atomic radii and electronegativity of both 4*f* electron localized and itinerant Ce in the *fcc*-Ce<sub>3</sub>Al alloy. The results are shown in the Darken–Gurry map using the Al atom as the reference (Figure 7.2). At

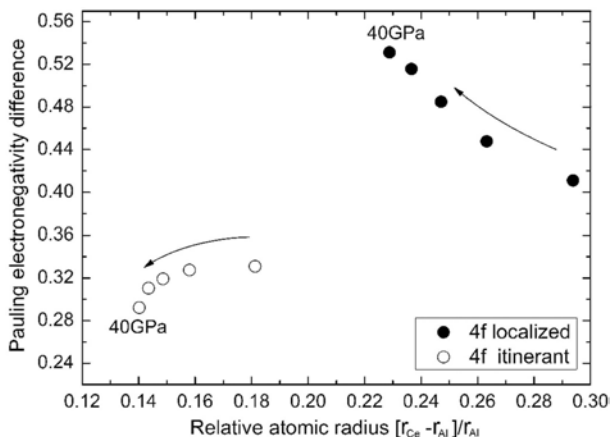


Figure 7.2: Darken–Gurry map of Ce in reference to Al calculated from theory. Results for pressures 0, 10, 20, 30, and 40 GPa are shown by circles (4*f* electron localized, filled; itinerant, open). Arrows indicate the direction of increasing pressure.

ambient pressure and temperature, the 4*f* localized Ce is clearly too different from Al in terms of both atomic size and electronegativity, thus preventing the alloying with Al. The larger compressibility of Ce compared with Al allows pressure to narrow the size difference between 4*f* electron localized Ce and Al, but the difference is still as large as 22% up to 40 GPa. In addition, pressure widens the difference in electronegativity between Al and 4*f* electron localized Ce and reduces the likelihood of forming a substitutional alloy.

However, 4*f* itinerant Ce has a much smaller radii which is within 18% of Al at zero pressure, and the differential compressibility between Ce and Al further reduces the difference to 15% at 20 GPa. In addition, the electronegativity of 4*f* electron itinerant Ce is much closer to Al and the negative pressure dependence brings them into even better agreement.

In summary, while the pressure–induced 4*f* electronic delocalization brings Ce and Al into compliance with the HR rules, making the random alloy possible, the release of pressure, and the consequent 4*f* localization, transforms it into a non–Hume–Rothery random alloy.

### 7.3 Structure of Li/Na–NH<sub>2</sub>BH<sub>3</sub>

In Paper XIV the structure of LiNH<sub>2</sub>BH<sub>3</sub> and NaNH<sub>2</sub>BH<sub>3</sub> is determined. Ammonia borane (NH<sub>3</sub>BH<sub>3</sub>) has been suggested as a chemical hydrogen

storage material, mainly due to its favourable gravimetric and volumetric properties [146–150]. The release of hydrogen results in polymerization to  $(\text{NH}_2\text{BH}_3)_n$  and eventually to  $(\text{NHBH})_n$ . The rapid polymerization poses a problem for rehydrogenation. Furthermore, the released hydrogen is contaminated with aminoborane and trace quantities of borazine [146–150]. Recently, Xiong *et al.* [151] reported that the amidoboranes  $\text{LiNH}_2\text{BH}_3$  and  $\text{NaNH}_2\text{BH}_3$  provide high storage capacity (10.9 and 7.5 wt%, respectively) of hydrogen at easily accessible temperatures without the unwanted release of borazine. The production of  $\text{LiNH}_2\text{BH}_3$  and  $\text{NaNH}_2\text{BH}_3$  is based on the following reactions:



Much remains to be understood about these materials as  $\text{LiNH}_2\text{BH}_3$  and  $\text{NaNH}_2\text{BH}_3$  compounds have not yet been studied in greater detail in the literature. Here we focus on the ground-state properties and crystal structures of both  $\text{LiNH}_2\text{BH}_3$  and  $\text{NaNH}_2\text{BH}_3$  and analyze the energetics of their respective hydrogen desorption processes from first principles.

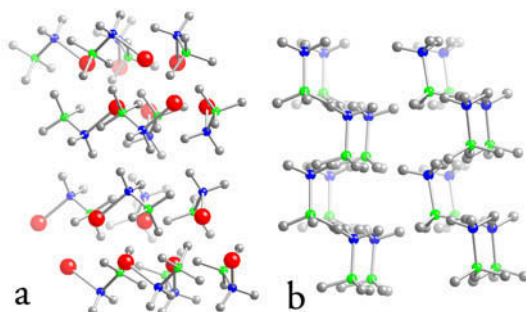


Figure 7.3: The fully relaxed crystal structures of (a)  $\text{LiNH}_2\text{BH}_3$  and (b)  $\text{NH}_3\text{BH}_3$  as obtained from our density functional theory calculation. Li is shown as red spheres, N in blue, B in green, and H in gray

We initiated our investigation by first determining the ground-state crystal structure of both  $\text{LiNH}_2\text{BH}_3$  and  $\text{NaNH}_2\text{BH}_3$  from *ab initio* calculations. The single-molecule geometries of  $\text{LiNH}_2\text{BH}_3$  and  $\text{NaNH}_2\text{BH}_3$  were optimized using a localized basis set. The resulting atomic positions were then used to set reasonable starting values for the fractional coordinates  $x$ ,  $y$ , and  $z$  of all atoms in the space group  $Pbca$  from which a full relaxation of the crystal structure then was carried out. Although the experiment [151] determined the space group of  $\text{LiNH}_2\text{BH}_3$  with near-100% certainty, we attempted to perform a theoretical test of how stable the  $Pbca$  phase of  $\text{LiNH}_2\text{BH}_3$  is, compared to competing structures. In the following, we list the space groups and their respective total energy difference in eV/f.u. relative to the  $Pbca$  phase in parentheses:  $Pbcn$ (0.42),  $Pnma$ (0.48),  $Pcca$ (0.86), and  $Pnnm$ (2.27). Based on these results, we are able to confirm that the  $Pbca$  structure does indeed

yield the lowest total energy, among the tested structures, and is stabilized by 0.42 eV/f.u. against the second most stable phase *Pbcn*. Calculations of the vibrational spectrum at the  $\Gamma$  point yielded information about a possible existence of soft modes in the *Pbca* structure. No imaginary frequencies were found, suggesting that the structure is dynamically stable. Our theoretically determined lattice parameters,  $a=7.108$  Å,  $b=13.945$  Å, and  $c=5.150$  Å, for  $\text{LiNH}_2\text{BH}_3$  are in excellent agreement with those obtained experimentally, namely,  $a=7.11274$  Å,  $b=13.94877$  Å, and  $c=5.15018$  Å. For  $\text{NaNH}_2\text{BH}_3$ , our theoretically determined lattice parameters are virtually identical to those obtained experimentally [151], namely,  $a=7.46931$  Å,  $b=14.65483$  Å, and  $c=5.65280$  Å. A schematic of the crystal structure of  $\text{LiNH}_2\text{BH}_3$  is shown in Figure 7.3. The optimized geometry appears virtually identical to the structural figures provided in Ref. [151]. Regarding the internal structure of the  $\text{LiNH}_2\text{BH}_3$  units forming the crystal: the Li–N and N–B bond lengths are found by us to be 2.02 and 1.55 Å, respectively, in very good agreement with the experimental results of 1.98 and 1.56 Å, respectively.

## 7.4 Phase-change materials

Phase-change materials (PCM) are highly interesting for data-storage applications [6]. Data stored in phase change materials is non-volatile, *i.e.* not requiring power to remain in the stored state. Crystalline and amorphous regions of the material represent the binary encoding of the data. The two states can be distinguished either optically, through the difference in reflectivity, or electronically, through the difference in resistance. Except for the key property of having distinguishable phases, a PCM requires fast switching, on the order of tens of nanoseconds, between the two phases in order to be used in storage applications. However, a full understanding of the phase-change mechanism has not yet been achieved although PCMs are commercially used. Therefore, it is of interest to study the amorphous and liquid structures.

### 7.4.1 Local structure of liquid and amorphous $\text{Ge}_1\text{Sb}_2\text{Te}_4$

In Paper XV and XVI, we explore the local structure of liquid and amorphous  $\text{Ge}_1\text{Sb}_2\text{Te}_4$ .

The crystalline  $\text{Ge}_1\text{Sb}_2\text{Te}_4$  (GST-124) was first melted at 3000 K, and then gradually quenched. The data for the molten structure was gathered at 1000 K, which is well above the melting temperature of GST-124, and the data for the amorphous structure was gathered at 300 K. In Figure 7.4, the distribution of coordination numbers of each species, for the crystalline, liquid, and amorphous GST-124 is shown. In general, the coordinations of the liquid and amorphous state are lower than those of the crystalline phase. Moreover, we can see that the liquid and amorphous coordinations look rather

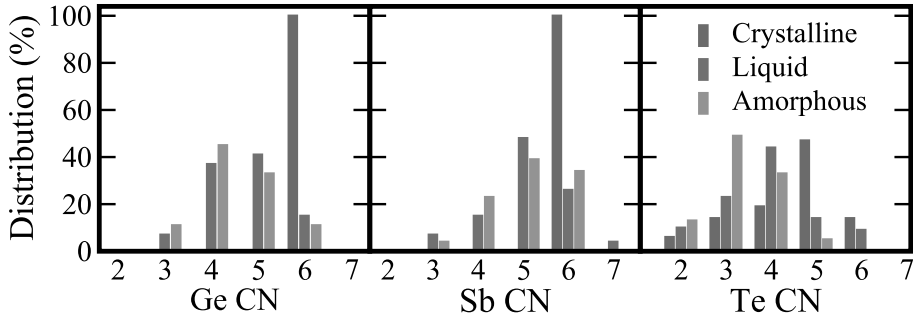


Figure 7.4: Distribution of coordination numbers for crystalline, liquid, and amorphous GST-124

similar. If we look at the BAD, plotted in Figure 7.5, however, we find a local geometry which resembles the crystalline geometry.

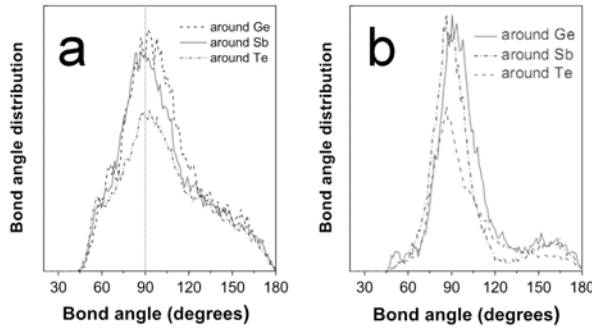


Figure 7.5: Bond angle distribution for liquid and amorphous GST-124

In both cases, we can see a big contribution from an octahedral symmetry, which manifest itself as angles around  $90^\circ$ , and close to  $180^\circ$  (In the crystalline case, it would be exactly  $90^\circ$  and  $180^\circ$ ). A smaller contribution of tetrahedral symmetry can be observed as a small shoulder around  $109^\circ$ . The small peak at  $60^\circ$  is interpreted as triangular rings. The resemblance of the local geometries of the liquid and amorphous structures with the crystalline structure may play a key role in the fast switching between the crystalline and the amorphous state.

#### 7.4.2 N-doping of $\text{Ge}_2\text{Sb}_2\text{Te}_5$

In Paper XVII, we investigate the local structure around nitrogen in N-doped  $\text{Ge}_2\text{Sb}_2\text{Te}_5$ . Using  $\text{Ge}_2\text{Sb}_2\text{Te}_5$  as a memory device [6, 152], requires a reduction of power consumption in order to compete with other memory types, such as flash memories based on floating-gate transistors. Nitrogen doping has been shown to be an efficient way of reducing the power consumption of

$\text{Ge}_2\text{Sb}_2\text{Te}_5$  [153, 154]. In N-doped amorphous GST (*a*-NGST), N was reported to exist in the form of  $\text{GeN}_x$  and  $\text{N}_2$  [153, 154]. For practical applications, the stability of  $\text{GeN}_x$  and  $\text{N}_2$  is critical, since poor stability will lead to performance degradation.

We used supercells containing 24 Ge, 24 Sb, 60 Te, and 12 N atoms, constructed from cubic GST-225. The 10% N doped GST-225 is close to what is used experimentally [153, 154]. We used two different densities, namely that of 0 K relaxed amorphous NGST ( $\rho_L = 5.7 \text{ g/cm}^3$ , referred to as *La*-NGST), and that of the cubic crystalline phase ( $\rho_H = 6.37 \text{ g/cm}^3$ , referred to as *Ha*-NGST phases). First, the two systems were melted and thermalized at 5000 K for 3 ps to completely eliminate the memory of their original structures. The liquids were then quenched down to 300 K by a quenching rate of  $333 \text{ K ps}^{-1}$ , followed by a re-thermalization of 3 ps at 300 K. To check the stability of the quenched structures, they were heated to 600 K, where the simulations were run for 30 ps.

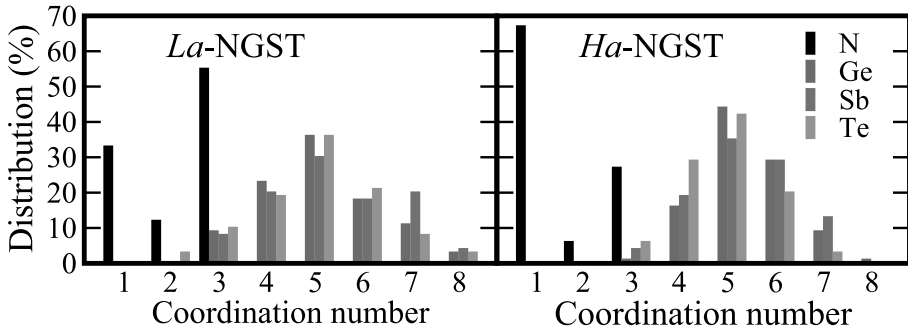


Figure 7.6: Distribution of coordination numbers for low (*La*-NGST) and high (*Ha*-NGST) density N-doped GST-225

In Figure 7.6, the resulting coordination of the quenched structures is displayed. Both  $\text{N}_2$  and  $\text{Ge}(\text{Sb}, \text{Te})\text{N}$  complexes are found in the quenched structures. Furthermore, comparing the two densities, indicate that the formation of  $\text{N}_2$  could be enhanced by the higher density. More statistics would however be required to solidify this result. The  $\text{N}_2$  remained unaffected by the re-heating to 600 K, but did result in some internal re-organizations among the  $\text{Ge}(\text{Sb}, \text{Te})\text{N}$  complexes.

#### 7.4.3 Clustering of vacancies in $\text{Ge}_2\text{Sb}_2\text{Te}_5$

In Paper XVIII we investigate how the density can affect the amorphous GST-225. To investigate the effect of pressure, two densities have been used, the experimental density of  $0.0297 \text{ atoms/\AA}^3$  [155] for amorphous GST-225, and  $0.0348 \text{ atoms/\AA}^3$ , the theoretical density for crystalline GST-225 obtained from an *ab initio* calculation at 0 K. The structures were melted at 3000 K for 3 ps, and then quenched to 300 K with a rate of  $6.6 \text{ K ps}^{-1}$ . The amorphous structures were run at 300 K for 3 ps, to gather the structural data for the

amorphous structure. The low and high density amorphous structures are denoted *La*-GST and *Ha*-GST, respectively. The resulting pressure in the *La*-GST and *Ha*-GST at 300 K was 1.2 kbar and 26 kbar, respectively.

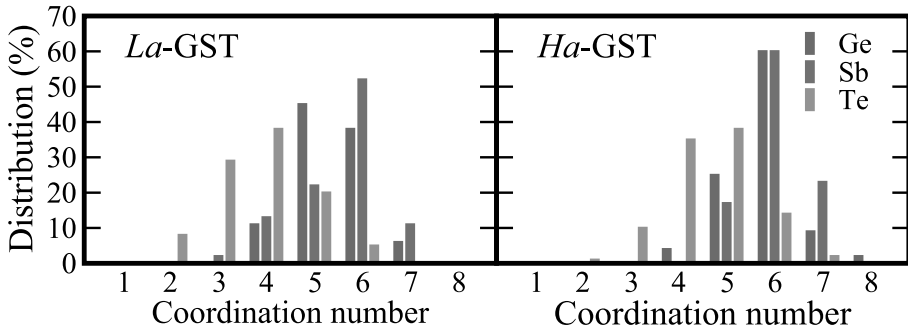


Figure 7.7: Distribution of coordination numbers for low (*La*-GST) and high (*Ha*-GST) density GST-225

The coordination of the two structures are shown in Figure 7.7. As can be seen, the pressure difference results in a shift to higher coordination with increased pressure. We can also see that in contrast to the N-doped GST-225 (see Figure 7.6), where the coordination was rather homogenous (for Ge, Sb, and Te), we here see that Te has lower coordination. In fact, in *La*-GST the low coordinated Te surround clusters of vacancies. This clustering of vacancies disappears as the density is increased (*Ha*-GST).

#### 7.4.4 Phase stability of $m\text{InSb} \cdot n\text{InTe}$

In Paper XIX the phase stability of  $m\text{InSb} \cdot n\text{InTe}$  is investigated. As a non-GST phase-change alloy,  $\text{In}_3\text{SbTe}_2$  (IST-312) with a NaCl structure was shown to have the potential use as a reversible optical data storage media, with high-speed erasing and long-term data retention [156–158]. In contrast to rock-salt structured GST alloys, where Ge, Sb, and vacancies randomly occupy the Na sites, and Te occupies the Cl sites [159, 160], both sites in IST-312 has random occupation, i.e., In and vacancies occupy the Na sites while Sb, Te, and vacancies occupy the Cl sites. In GST system, both  $\text{Ge}_1\text{Sb}_2\text{Te}_4$  and  $\text{Ge}_2\text{Sb}_2\text{Te}_5$  can be considered as pseudo-binary  $m\text{GeTe} \cdot n\text{Sb}_2\text{Te}_3$  alloys which are in the GeTe– $\text{Sb}_2\text{Te}_3$  tie line [159]. Similar to GST alloys system, IST-312 can also be considered as a pseudo-binary  $m\text{InSb} \cdot n\text{InTe}$  alloy in the InSb–InTe tie line [161]. In addition, rock-salt structured  $\text{In}_4\text{SbTe}_3$  (IST-413), another alloy in the InSb–InTe tie line, can be considered as having In occupying the vacancies at Na sites and Te occupying the vacancies at Cl sites of IST-312.

In order to investigate the stability of IST-312 and IST-413, we have calculated the enthalpy of formation with InSb and InTe as references. The random site occupation was modelled by generating special quasi-random structures (SQS) [162], which tries to mimics the radial distribution function of a perfectly random alloy. The enthalpy of formation is +0.258 eV/atom for

IST-312, and +0.043 eV/atom for IST-413. The positive enthalpy of formation indicates that crystalline IST-312 is a metastable phase and could decompose to InSb and InTe. Experimentally, IST-312 formed at 360–400 °C [158, 163] and decomposed to InSb and InTe under slow cooling from 450 °C [156]. The less positive enthalpy of formation of IST-413 suggests that it is more stable than IST-312. Temperature, in the form of configurational entropy, will however have a more stabilizing effect on IST-312, since IST-413 is a structure without vacancies, and only has random occupation on one of the sub-lattices.

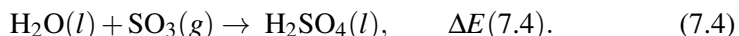
## 7.5 Cars start due to relativity

In Paper XX, the relativistic effects on the discharge reaction of the lead-acid is investigated. The lead battery is an essential part of cars, and has numerous other applications. This well-known invention is now 150 years old [164, 165]. About 75% of the World lead production and a turnover of about 30 billion USD are due to these batteries [166]. In contrast to other batteries, the lead battery contains a heavy-element, Pb, where relativistic effects on its compounds could play an important role, as qualitatively found a long time ago [167–170]. For metallic lead, see [171–173].

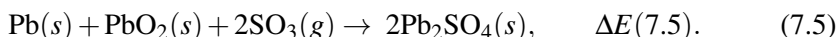
The lead-acid battery[174] has a positive lead dioxide electrode, a negative electrode of metallic lead, and a sulphuric acid electrolyte. The discharge reaction between a Pb(IV) and a Pb(0) produces 2 Pb(II), in form of solid PbSO<sub>4</sub>. The experimental thermodynamics of the reaction are well-known [175]. The discharge reaction of the lead-acid cell is



The three solids can be treated with DFT. Adequately simulating the liquid phase in multiple relativistic regimes is beyond current state of the art, however. We avoid this problem by introducing the known energy  $\Delta E(7.4)$  for the experimental reaction



We can use this empirical relationship because only light elements and only S(VI) occur in Equation 7.4, whose contribution to relativistic effects are small. Combining Equations 7.3 and 7.4 gives



The voltages for the lead-acid battery reaction may then be calculated from the reaction energies

$$\Delta E(7.3) = \Delta E(7.5) - 2\Delta E(7.4), \quad (7.6)$$

where we use calculated  $\Delta E(7.5)$  values and experimental  $\Delta E(7.4)$  values [175].

The calculations are performed with crystal structures from experimental room-temperature measurements, allowing no ionic relaxations, thus capturing the electronic effects of relativity (meaning Dirac vs. Schrödinger).

Table 7.1: *Comparison of the experimental and calculated results for the EMF [V] of the lead-battery reaction (1).*

Method		Level of relativity			$\Delta$	$\Delta$
		NR	SR	FR	FR-NR	SR-NR
BAND	VWN	+0.55	+2.52	+2.27	+1.72	+1.97
	PBEsol-D	+0.21	+2.25	+2.02	+1.81	+2.04
FPLO	PW92	+0.41	+2.20	+2.10	+1.69	+1.80
	PW92b	+0.39	+2.21	+2.11	+1.72	+1.82
	Av.	+0.39	+2.30	+2.13	+1.74	+1.91
	Exp. <sup>a</sup>			+2.107		

<sup>a</sup> Ref. [176]

The resulting reaction energies for the lead battery reaction 7.3, calculated at the FR (fully relativistic), SR (scalar relativistic = without spin-orbit coupling), and NR (non-relativistic) levels are compared to experiment in Table 7.1. We manage to reproduce the absolute voltage of the lead battery reaction within about 0.2 V. Taking the four calculations in Table 7.1 at face value, our calculated absolute voltage for reaction (7.3), in  $\text{H}_2\text{SO}_4 \cdot 10\text{H}_2\text{O}$ , is +2.13 V while its relativistic part is +1.74 V. This finding is consistent with the fact that no corresponding 'tin battery' exists, where the relativistic effects are much smaller [177]. In short, this means that cars start due to relativity.



## 8. Conclusions and Outlook

*I am now convinced that theoretical physics is actually philosophy.*

— Max Born

IN THIS THESIS, density functional theory and *ab initio* molecular dynamics have been employed to improve our understanding of the atomic details that is the origin of materials properties. Mainly four classes of properties have been studied: diffusion, adsorption, catalysis, and structure.

Hydrogen interaction with transition metals seem at a first glance to be rather simple. When we look more closely however, hydrogen induces a self-trapped state, which has big consequences for the diffusion properties, both in the quantum and in the classical regime. Furthermore, the interaction of the polaron quasi-particles, will have a big influence on the metal-hydrogen phase diagrams. It would be worthwhile to try to quantify this interaction.

Diffusion of Li in the Li-N-H systems show a manifold of interesting behaviours. In  $\text{Li}_3\text{N}$ , the diffusion is controlled by the concentration of Li vacancies, and is mainly limited to two dimensions in the crystal. In  $\text{Li}_2\text{NH}$ , the diffusion is not dependent on vacancies, but is instead controlled by rotations of NH units, which starts to rotate at a phase transition at 385 K. In  $\text{LiNH}_2$ , the diffusion requires both Li vacancies and rotations of the  $\text{NH}_2$  units. This however, does not occur until  $\sim 700$  K. A possibility to lower the transition temperature of the superionic transition in  $\text{Li}_2\text{NH}$  could be through doping with large ions, opening up the structure and lowering the barrier for NH rotations.

Adsorption of hydrogen in high-surface area materials, *e.g.* MOF or COF, exhibits too low adsorption energies ( $\sim 5$  kJ/mol  $\text{H}_2$ ) due to weak van der Waals interactions. To store the hydrogen at room temperature and ambient pressure would require adsorption energies around 40 kJ/mol  $\text{H}_2$ . Li-decoration increases the adsorption energy, but only comes half way to the room temperature requirement. Transition metal decoration, which could strengthen the adsorption further, has problems with metal clustering. Finding a way to anchor, and synthesize, transition metal decoration would be a highly interesting way to pursue increased adsorption energies.

Transition metal dopants in  $\text{NaAlH}_4$  and  $\text{NaBH}_4$  exhibit a high affinity for Al. Furthermore, the hydrogens surrounding the transition metal have decreased binding energies as well as increased hydrogen mobility. Our results support the proposed idea that the catalytic mechanism is related to the formation of an intermetallic transition metal-aluminum phase. Carbon

nanostructures are shown to display similar catalytic effects for hydrogen desorption in  $\text{NaAlH}_4$ . This effect is shown to be due to the high electron affinity of the carbon substrates, destabilizing the  $\text{AlH}_4$  units. Pursuing the catalytic mechanism behind hydrogen re-absorption, for both transition metals and carbon nanostructure, would be a way to gain knowledge which would be important for the whole field of chemical hydrides.

Ground state structure determination through an *ab initio* random structure search yields a new structure for both  $\text{BeC}_2$  and  $\text{MgC}_2$ . The developed space group optimized random structure search method is estimated to lower the computational cost by an order of magnitude, due to the decreased size of the Brillouin zones, as compared to a completely random search algorithm.

The fast crystallization time of GeSbTe phase-change materials is attributed to the close resemblance between the liquid/amorphous structures and the crystalline structures.

Finally, as an example of every day relativity, we show that the voltage in lead-acid batteries is due to relativistic effects in the lead compounds.

## 9. Acknowledgement

*I can't think that it would be terrible of me to say — and it is occasionally true — that I need physics more than friends.*

— J. Robert Oppenheimer

THIS THESIS is the result of the last few years of work, not only by my, but also by everybody who have helped me. Therefor, I would like to take the opportunity to thank those people.

Rajeev, for giving me the possibility to start my PhD studies in the materials theory group. Börje, for your smile, always spreading a good mood. I would like to thank my fellow explorers of hydrogen storage materials. Moysés, for all the great discussions over coffee, from which new ideas emerged almost every day. Ralph, for always having a positive attitude, and being so easy to work with. Pornjuk, for your hard work especially when nothing seemed to work. Gunnar and Björgvin, for giving me a different viewpoint, for the enthusiasm in our long discussions, and especially the more philosophical discussions on the fine structure of matter, which I enjoyed a lot. Cecilia, Duck, and Peter for all our good discussions, on amorphous, databases, optimization, phonons, and many other things. Andri and Hannes, for a tour into the world of instantons and tunnelling, and for the warm welcome to Iceland. I would like to thank all my other collaborators Li Wen, Puru, Ping Chen, Ragaiy, Pekka, Patryk, Zhimei, Fredrik, Sebastian, Ramzan, Mao, Wei, and everybody else. Elisabeth, for the views and help with university bureaucracy. Love, for the lunch table entertainment. Oscar, for the fun time in the course lab. I would like to thank Cecilia, Moysés, Ralph, and Peter for critically reading and commenting on this thesis. My family, all of you, for your warm support, most of all Moa, for your patience and encouragement. And to all my friends, for proving Oppenheimer wrong. Finally, I would like to thank everyone who thought this thesis looked interesting enough to open, and perhaps read.



## 10. Summary in Swedish

*Tänka fritt är stort men tänka rätt är större.*

— *Thomas Thorilds*

GENOM HISTORIEN har utvecklingen av mänskligheten varit nära kopplad till de material som använts under tidsperioden, t.ex. stenåldern, bronsåldern och järnåldern. Idag *upptäcker* vi inte bara nya material, utan försöker aktivt också *utveckla* nya material. Detta kräver en allt djupare förståelse för hur materien uppför sig. Ett av verktygen vi kan använda oss av i denna jakt på förståelse är kvantmekaniska beräkningar och simuleringar som utförs på stora superdatorer. I denna avhandling har kvantmekaniska beräkningar och *ab initio* molekylodynamiksimuleringar använts för detta ändamål.

Ett forskningsområde med många utmanande problem är lagring av väte i fasta material. Efterfrågan på energi ökar över hela världen, samtidigt är resursen av fossila bränslen begränsad och effekten av växthusgaser betraktas samtidigt som ett växande hot mot vår miljö. Därför söks nya vägar för att ersätta de fossila bränslena, såsom användningen av vätgas som ett syntetiskt bränsle. En av de avgörande frågorna som behöver lösas för att möjliggöra användande av vätgas som syntetiskt bränsle är att hitta ett material med de rätta egenskaperna för att lagra den. För att vätgas skall bli praktiskt användbart i transportbranschen krävs att lagringsmaterialet klarar av att ta upp tillräckligt stora mängder väte, både vikt och volymmässigt. Detta begränsar vilka grundämnen som kan användas till den övre delen av det periodiska systemet. I övrigt måste lagringen vara kostnadseffektivt, inte ge ifrån sig gifter och vara säker. Det praktiska användandet av ett lagringsmaterial kräver också att vätgasen går att extrahera tillräckligt snabbt och det vid en temperatur som inte är alldeles för hög.

Informationslagring är ett område som kontinuerligt kräver allt högre lagringstäthet. Mobil utrustning kräver samtidigt att lagringsminnet använder energin effektivt. Fasomvandlingsmaterial, som redan används kommersiellt, kan användas för att lagra data utan att det krävs en spänning för att behålla informationen, både i optisk lagring, t.ex. CD eller DVD, och i elektriska RAM-minnen. Fasomvandlingsmaterial har tydliga skillnader, både i optiska och elektriska egenskaper, mellan deras kristallina och amorfa faser. Den snabba kristallisationen som sker i dessa material, är en förutsättning för att de skall kunna användas för lagring av information. Om man förstår den snabba kristallisationen skulle det finnas möjligheter att hitta nya fasomvandlingsmaterial som förbrukar mindre energi.

Avhandlingen är uppdelad på fyra underområden, diffusion, adsorption, katalys och struktur.

Interaktionen mellan väte och en övergångsmetall kan vid första anblicken verka vara ganska enkel. Men en närmare studie visar att vätet inducerat en lokalisering av en elektron, vilket i sin tur leder till en potentialgrop för vätet jämfört med den omgivande metallen. Detta visar sig ha stora konsekvenser för diffusionen av väte, både i temperaturregioner där diffusionen är kvantmekanisk och där den är klassisk. Samspelet mellan töjningsfälten som skapas på grund av denna mekanism måste ha stor betydelse för fasdiagram hos metall-väte system. Att försöka kvantisera denna växelverkan vore nästa steg i detta arbete.

Diffusionen av litium i Li-N-H har ett flertal intressanta beteenden. Hos  $\text{Li}_3\text{N}$ , bestäms diffusionshastigheten av mängden vakanser. Dessutom förekommer diffusionen främst i två dimensioner. I  $\text{Li}_2\text{NH}$ , är inte diffusionen längre beroende av vakanser, utan styrs istället av rotationer hos NH bindningarna, som börjar rotera vid en fasövergång vid 385 K. I  $\text{LiNH}_2$ , kräver diffusionen både vakanser och rotationer av  $\text{NH}_2$ . Detta inträffar dock inte förrän 700 K. Det skulle vara mycket intressant att undersöka om övergångstemperaturen i  $\text{Li}_2\text{NH}$  skulle gå att sänka genom dopning med stora joner, för att öppna upp strukturen och minska barriären som begränsar NH rotationerna.

Adsorption av vätgas på ytan hos nanoporösa material, t.ex. MOF eller COF, har en låg adsorptionsenergi ( $\sim 5$  kJ/mol  $\text{H}_2$ ). Att binda väte vid rumstemperatur skulle det krävas adsorptionsenergies kring 40 kJ/mol  $\text{H}_2$ . Genom att dekorera materialen med  $\text{Li}^+$  joner kan adsorptionsenergin ökas till 12–18 kJ/mol  $\text{H}_2$ , men detta räcker inte för lagring av väte vid rumstemperatur. En möjlighet att förbättra växelverkan skulle vara att tillföra övergångsmetaller, det tillför dock problem med anhopningar av metallen, vilket leder till att man inte får någon förbättring av adsorptionsegenskaperna.

Orenheter i form av övergångsmetaller i  $\text{NaAlH}_4$  och  $\text{NaBH}_4$  visar sig ha stor attraktion för aluminiumatomer. I övrigt visar det sig att väteatomer kring orenheterna har större rörlighet jämfört med väteatomer i andra delar av materialet. Våra resultat stöder en föreslagen hypotes om att den katalytiska mekanismen för adsorption och desorption av väte är relaterad till bildandet av en intermetalliska övergångsmetall-aluminiumlegering. Kolnanostrukturer visas ha samma katalytisk effekt för desorption av vätgas från  $\text{NaAlH}_4$ .

Bestämning av ett materials grundtillstånd med hjälp av slumpmässing sökning hittade nya grundtillstånd för både  $\text{BeC}_2$  och  $\text{MgC}_2$ . Den utvecklade metoden som optimerats genom att ta rymdgruppssymmetrier i beaktande beräknas sänka datortiden som krävs med en storleksordning, på grund av minskad storlek på de irreducibla Brillouinzonerna.

Simuleringar av vätske- och amorffas hos GeSbTe antyder att den snabba kristalliseringstiden kan bero på de stora likheterna hos den lokala strukturen med den kristallina strukturen.

Slutligen visar vi som ett exempel på vardaglig relativitetsteori att bilen startar på grund av relativistiska effekter. Blybatteriet skulle nämligen inte ha sin spänning utan relativistiska effekter.



# Table of Acronyms

<b>AIMD</b>	<i>Ab Initio</i> Molecular Dynamics	8
<b>AIRS</b>	<i>Ab Initio</i> Random Search	51
<b>BAD</b>	Bond Angle Distribution	12
<b>BOD</b>	Bond Orientation Distribution	13
<b>CMD</b>	Classical Molecular Dynamics	9
<b>COF</b>	Covalent Organic Frameworks	31
<b>DFT</b>	Density Functional Theory	4
<b>GGA</b>	Generalized Gradient Approximation	5
<b>HR</b>	Hume-Rothery rules	52
<b>HTST</b>	Harmonic Transition State Theory	16
<b>LDA</b>	Local Density Approximation	5
<b>MD</b>	Molecular Dynamics	9
<b>MOF</b>	Metal Organic Frameworks	31
<b>MSD</b>	Mean Square Displacement	11
<b>NEB</b>	Nudged Elastic Band method	27
<b>PAW</b>	Projector Augmented-Wave method	7
<b>PCM</b>	Phase-Change Material	56
<b>RDF</b>	Radial Distribution Function	10
<b>SQS</b>	Special Quasi-random Structure	59

<b>TST</b>	Transition State Theory	16
<b>VACF</b>	Velocity Auto–Correlation Function	13
<b>VSD</b>	Vibrational Spectral Density	13
<b>ZPE</b>	Zero–Point Energy	17

# Bibliography

- [1] Turner, J. A. *Science* **285**, 687 (1999).
- [2] Crabtree, G. W., Dresselhaus, M. S., and Buchanan, M. V. *Phys. Today* **57:12**, 39 (Dec 2004).
- [3] Schlapbach, L. and Züttel, A. *Nature* **414**, 353 (2001).
- [4] Yang, J., Sudik, A., Wolverton, C., and Siegel, D. J. *Chem. Soc. Rev.* **39**, 656 (2010).
- [5] Grochala, W. and Edwards, P. P. *Chem. Rev.* **104**, 1283 (2004).
- [6] Wuttig, M. and Yamada, N. *Nature Mater.* **6**, 824 (2007).
- [7] Born, M. and Oppenheimer, J. *Ann. Physik* **84**, 457 (1927).
- [8] Hohenberg, P. and Kohn, W. *Phys. Rev.* **136**, B 864 (1964).
- [9] Kohn, W. and Sham, L. J. *Phys. Rev.* **140**, A 1133 (1965).
- [10] Becke, A. D. *Phys. Rev. A* **38**, 3098 (1988).
- [11] Perdew, J. P. and Wang, Y. *Phys. Rev. B* **45**, 13244 (1992).
- [12] Perdew, J. P., Burke, K., and Ernzerhof, M. *Phys. Rev. Lett.* **77**, 3865 (1996).
- [13] Kittel, C. *Introduction to Solid State Physics*. John Wiley and Sons, (1996).
- [14] Blöchl, P. E. *Phys. Rev. B* **50**, 17953 (1994).
- [15] Hamann, D. R., Schlüter, M., and Chiang, C. *Phys. Rev. Lett.* **43**, 1494 (1979).
- [16] Andersen, O. K. *Phys. Rev. B* **12**, 3060 (1975).
- [17] Martin, R. M. *Electronic Structure, Basic Theory and Practical Methods*. Cambridge University Press, Cambridge, (2004).
- [18] Car, R. and Parrinello, M. *Phys. Rev. Lett.* **55**, 2471 (1985).
- [19] Alder, B. J. and Wainwright, T. E. *Phys. Rev. A* **1**, 18 (1970).
- [20] Alefeld, G. and Vökl, J. *Hydrogen in Metals I*. Springer-Verlag Berlin, (1978).
- [21] Alefeld, G. and Vökl, J. *Hydrogen in Metals II*. Springer-Verlag Berlin, (1978).
- [22] Wipf, H. *Hydrogen in Metals III*. Springer-Verlag Berlin, (1997).

- [23] Fukai, Y. *The Metal-Hydrogen System: Basic Bulk Properties*. Springer-Verlag Berlin, (2005).
- [24] Eguchi, T. and Morozumi, S. *Nippon Kinzokugakkaishi* **41**, 795 (1977).
- [25] Qi, Z., Völkl, J., Lässer, R., and Wenzl, H. *J. Phys. F* **13**, 2053 (1983).
- [26] Fukai, Y. *Jpn. J. Appl. Phys.* **22**, 207 (1983).
- [27] Andersson, P. H., Fast, L., Nordström, L., Johansson, B., and Eriksson, O. *Phys. Rev. B* **58**, 5230 (1998).
- [28] Li, Y. G. and Wahnström, G. *Phys. Rev. B* **51**, 12233 (1995).
- [29] Sundell, P. G. and Wahnström, G. *Phys. Rev. Lett.* **92**, 1 (2004).
- [30] Sundell, P. G. and Wahnström, G. *Phys. Rev. B* **70**, 224301 (2004).
- [31] Hempelmann, R. *J. Less Common Met.* **101 IS**, 69 (1984).
- [32] Schober, H. R. and Stoneham, A. *Phys. Rev. Lett.* **60**, 2307 (1988).
- [33] Stoneham, A. M., Gavartin, J., Shluger, A. L., Kimmel, A. V., Ramo, D. M., Ronnow, H. M., Aepli, G., and Renner, C. *J Phys. Cond. Matter* **19**, 255208 (2007).
- [34] Wahnström, G. and Li, Y. G. *Phys. Rev. Lett.* **71**, 1031 (1993).
- [35] Dosch, H. and Peisl, J. *Phys. Rev. Lett.* **56**, 1385 (1986).
- [36] Dosch, H., Peisl, J., and Dorner, B. *Phys. Rev. B* **35**, 3069 (1987).
- [37] Dosch, H., Schmid, F., Wiethoff, P., and Peisl, J. *Phys. Rev. B* **46**, 55 (1992).
- [38] Juza, R. and Opp, K. *Z. Anorg. Allg. Chem.* **266**, 325 (1951).
- [39] Juza, R. and Opp, K. *Z. Anorg. Allg. Chem.* **266**, 313 (1951).
- [40] Chen, P., Xiong, Z., Luo, J., Lin, J., and Tan, K. L. *Nature* **420**, 302 (2002).
- [41] Ichikawa, T., Hanada, N., Isobe, S., Leng, H., and Fujii, H. *J. Phys. Chem. B* **108**, 7887 (2004).
- [42] Miwa, K., Ohba, N., Towata, S., Nakamori, Y., and Orimo, S. *Phys. Rev. B* **71**, 195109 (2005).
- [43] Herbst, J. F. and Jr., L. G. H. *Phys. Rev. B* **72**, 125120 (2005).
- [44] Noritake, T., Nozaki, H., Aoki, M., Towata, S., Kitahara, G., Nakamori, Y., and Orimo, S. *J. Alloys Compd.* **393**, 264 (2005).
- [45] Ohoyama, K., Nakamori, Y., Orimo, S., and Yamada, K. *J. Phys. Soc. Jpn.* **74**, 483 (2005).
- [46] Magyari-Köpe, B., Ozoliņš, V., and Wolverton, C. H. *Phys. Rev. B* **73**, 220101 (2006).

- [47] Balogh, M. P., Jones, C. Y., Herbst, J. F., Jr., L. G. H., and Kundrat, M. *J. Alloys Compd.* **420**, 326 (2006).
- [48] Araujo, C. M., Scheicher, R. H., Jena, P., and Ahuja, R. *Appl. Phys. Lett.* **91**, 091924 (2007).
- [49] Araujo, C. M., Scheicher, R. H., and Ahuja, R. *Appl. Phys. Lett.* **92**, 021907 (2008).
- [50] Dresselhaus, M. S. and Thomas, I. L. *Nature* **414**, 332 (2001).
- [51] Rigden, J. S. *Hydrogen: The Essential Element*. Harvard Univ. Press, Cambridge, MA, (2003).
- [52] Grochala, W. and Edwards, P. P. *Chem. Rev.* **104**, 1283 (2004).
- [53] Alper, J. *Science* **299**, 1686 (2003).
- [54] Cortright, R. D., Davda, R. R., and Dumesic, J. A. *Nature* **418**, 964 (2002).
- [55] Rosi, N. L., Eckert, J., Eddaoudi, M., Vodak, D. T., Kim, J., O’Keeffe, M., and Yaghi, O. M. *Science* **300**, 1127 (2003).
- [56] Schlapbach, L. *Nature* **460**, 809 (2009).
- [57] Henkelman, G., Uberuaga, B., and Jonsson, H. *J. Chem. Phys.* **113**, 9901 (2000).
- [58] Mali, M., Roos, J., and Brinkmann, D. *Phys. Rev. B* **36**, 3888 (1987).
- [59] Beister, H. J., Haag, S., Kniep, R., Strossner, K., and Syassen, K. *Angew. Chem., Int. Ed. Engl.* **27**, 1101 (1988).
- [60] Lazicki, A., Maddox, B., Evans, W. J., Yoo, C. S., McMahan, A. K., Pickett, W. E., Scalettar, R. T., Hu, M. Y., and Chow, P. *Phys. Rev. Lett.* **95**, 165503 (2005).
- [61] Cui, S., Feng, W., Hu, H., Feng, Z., and Wang, Y. *Solid State Commun.* **149**, 612 (2009).
- [62] v. Alpen, U., Rabenau, A., and Talat, G. H. *Appl. Phys. Lett.* **30**, 621–623 (1977).
- [63] Armstrong, R. D., Dickinson, T., and Willis, P. M. *J. Electroanal. Chem.* **53**, 389–405 (1974).
- [64] Boukamp, B. A. and Huggins, R. A. *Mater. Res. Bull.* **13**, 23–32 (1978).
- [65] v. Alpen, U. *J. Solid State Chem.* **29**, 379–392 (1979).
- [66] v. Alpen, U. and Bell, M. F. *J. Electroanal. Chem.* **99**, 85–92 (1979).
- [67] v. Alpen, U., Bell, M. F., and Gladden, T. *Electrochim. Acta* **24**, 741–744 (1979).

- [68] Rea, J. R., Foster, D. L., Mallory, P. R., and Co, I. *Mater. Res. Bull.* **14**, 841–846 (1979).
- [69] Nishida, K., Asai, T., and Kawai, S. *Solid State Commun.* **48**, 701–704 (1983).
- [70] Sarnthein, J., Schwarz, K., and Blöchl, P. E. *Phys. Rev. B* **53**, 9084 (1996).
- [71] Wolf, M. L., Walker, J. R., and Catlow, C. R. A. *J. Phys. C: Solid State Phys.* **17**, 6623 (1984).
- [72] Wolf, M. L., Walker, J. R., and Catlow, C. R. A. *J. Phys. C: Solid State Phys.* **17**, 6635 (1984).
- [73] Ihara, A. and Suzuki, K. *Phys. Lett. A* **110**, 265 (1985).
- [74] Bader, B., Heitjans, P., Stockmann, H.-J., Ackermann, H., Buttler, W., Freilander, P., Kiese, G., van der Marel, C., and Schirmer, A. *J. Phys.: Condens. Matter* **4**, 4779 (1992).
- [75] Eddaoudi, M., Kim, J., Rosi, N., Vodak, D., Wachter, J., O’Keeffe, M., and Yaghi, O. M. *Science* **295**, 469 (2002).
- [76] Rowsell, J. L. C., Spencer, E. C., Eckert, J., Howard, J. A. K., and Yaghi, O. M. *Science* **309**, 1350 (2005).
- [77] Li, H., Eddaoudi, M., O’Keeffe, M., and Yaghi, O. M. *Nature* **402**, 276 (1999).
- [78] Mattesini, M., Soler, J. M., and Ynduráin, F. *Phys. Rev. B* **73**, 094111 (2006).
- [79] Rowsell, J. L. C., Millward, A. R., Park, K. S., and Yaghi, O. M. *J. Am. Chem. Soc.* **126**, 5556 (2004).
- [80] Rowsell, J. L. C. and Yaghi, O. M. *Angew. Chem. Int. Ed.* **44**, 4670 (2005).
- [81] Chae, H. K., Siberio-Pérez, D. Y., Kim, J., Go, Y., Eddaoudi, M., Matzger, A. J., O’Keeffe, M., and Yaghi, O. M. *Nature* **427**, 523 (2004).
- [82] Férey, G., Latroche, M., Serre, C., Millange, F., Loiseau, T., and Percheron-Guégan, A. *Chem. Comm.* , 2976 (2003).
- [83] Côté, A. P. and Shimizu, G. K. H. *Chem. Eur. J.* **9**, 5361 (2003).
- [84] Batten, S. R. and Robson, R. *Angew. Chem. Int. Ed.* **37**, 1460 (1998).
- [85] Chen, B., Eddaoudi, M., Hyde, S. T., O’Keeffe, M., and Yaghi, O. M. *Science* **291**, 1021 (2001).
- [86] Chen, B., Eddaoudi, M., Reineke, T. M., Kampf, J. W., O’Keeffe, M., and Yaghi, O. M. *J. Am. Chem. Soc.* **122**, 11559 (2000).
- [87] Lochan, R. C. and Head-Gordon, M. *Phys. Chem. Chem. Phys.* **8**, 1357 (2006).
- [88] Barbatti, M., Jalbert, G., and Nascimento, M. A. C. *J. Phys. Chem. A* **106**, 551 (2002).

- [89] Sun, Q., Jena, P., Wang, Q., and Marquez, M. *J. Am. Chem. Soc.* **128**, 9741 (2006).
- [90] Chen, P., Wu, X., Lin, J., and Tan, K. L. *Science* **285**, 91 (1999).
- [91] Froudakis, G. E. *Nano Lett.* **1**, 531 (2001).
- [92] Sagara, T., Klassen, J., and Ganz, E. *J. Chem. Phys.* **121**, 12543 (2001).
- [93] Henkelman, G., Arnaldsson, A., and Jónsson, H. *Comput. Mater. Sci.* **36**, 354 (2006).
- [94] Yildirim, T. and Hartman, M. R. *Phys. Rev. Lett.* **95**, 215504 (2005).
- [95] Mueller, T. and Ceder, G. *J. Phys. Chem. B.* **109**, 17974 (2005).
- [96] Yang, Q. and Zhong, C. *J. Phys. Chem. B* **109**, 11862 (2005).
- [97] Ceperly, D. M. and Alder, B. J. *Phys. Rev. Lett.* **45**, 566 (1980).
- [98] Panella, B., Hirscher, M., H.Pütter, and Müller, U. *Adv. Funct. Mater* **16**, 520 (2006).
- [99] Bushnell, J. E., Kemper, P. R., and Bowers, M. T. *J. Phys. Chem.* **98**, 2044 (1994).
- [100] Bogdanovic, B. and Schwickardi, M. *J Alloys Compd.* **253**, 1 (1997).
- [101] Hauback, B. C., Brinks, H. W., Jensen, C. M., Murphy, K., and Maeland, A. J. *J. Alloys Compd.* **358**, 142 (2003).
- [102] Thomas, G. J., Gross, K. J., Yang, N. Y. C., and Jensen, C. *J Alloys Compd.* **330**, 702 (2002).
- [103] Ozolins, V., Majzoub, E. H., and Udovic, T. J. *J. Alloys Compd.* **375**, 1 (2004).
- [104] Graetz, J., Reilly, J. J., Johnson, J., Ignatov, A. Y., and Tyson, T. A. *Appl. Phys. Lett.* **85**, 500 (2004).
- [105] Anton, D. L. *J Alloys Compd.* **356-357**, 400 (2003).
- [106] Brinks, H. W., Hauback, B. C., Srinivasan, S. S., and Jensen, C. M. *J. Phys. Chem. B* **109**, 15780 (2005).
- [107] Léon, A., Kircher, O., Fichtner, M., Rothe, J., and Schild, D. *J. Phys. Chem. B* **110**, 1192 (2006).
- [108] Aguayo, A. and Singh, D. J. *Phys. Rev. B* **69**, 155103 (2004).
- [109] Íñiguez, J. and Yildirim, T. *Appl. Phys. Lett.* **86**, 103109 (2005).
- [110] Íñiguez, J., Yildirim, T., Udovic, T. J., Sulic, M., and Jensen, C. M. *Phys. Rev. B* **70**, 060101 (2004).
- [111] Løvrvik, O. M. and Opalka, S. M. *Phys. Rev. B* **71**, 054103 (2005).

- [112] Løvvik, O. M. and Opalka, S. M. *Appl. Phys. Lett.* **88**, 161917 (2006).
- [113] Araújo, C. M., Ahuja, R., Guillén, J. M. O., and Jena, P. *Appl. Phys. Lett.* **86**, 251913 (2005).
- [114] Araújo, C. M., Li, S., Ahuja, R., and Jena, P. *Phys. Rev. B* **72**, 165101 (2005).
- [115] Li, Z., Morigazaki, N., Liu, B. H., and Suda, S. *J. Alloys Compd.* **349**, 232 (2003).
- [116] Li, Z., Liu, B. H., Arai, K., Morigazaki, N., and Suda, S. *J. Alloys Compd.* **356**, 469 (2003).
- [117] Li, Z., Liu, B. H., Arai, K., Asaba, K., and Suda, S. *J. Power Sources* **126**, 28 (2004).
- [118] Wu, C., Zhang, H., and Yi, B. *Catalysis Today* **93**, 477 (2004).
- [119] Woodley, S. M. and Catlow, R. *Nature Materials* **7**, 937 (2008).
- [120] Pickard, C. and Needs, R. *Phys. Rev. Lett.* **97**, 045504 (2006).
- [121] Pickard, C. and Needs, R. *Nature Physics* **3**, 473 (2007).
- [122] Pickard, C. and Needs, R. *Nature Materials* **7**, 775 (2008).
- [123] Yu, M., Louriea, O., Dyer, M. J., Moloni, K., Kelly, T. F., and Ruoff, R. S. *Science* **287**, 637 (2000).
- [124] Zhang, Y., Tang, T., Girit, C., Hao, Z., Martin, M. C., Zettl, A., Crommie, M. F., Shen, Y. R., and Wang, F. *Nature* **459**, 820 (2009).
- [125] Barone, V., Hod, O., and Scuseria, G. *Nano. Lett.* **6**, 2748 (2006).
- [126] Lieber, C. *Solid. State. Commun.* **107**, 607 (1998).
- [127] Xia, Y., Yang, P., Sun, Y., Wu, Y., Mayers, B., Gates, B., Yin, Y., Kim, F., and Yan, H. *Adv. Mater.* **15**, 353 (2003).
- [128] Yang, P., Yan, R., and Fardy, M. *Nano. Lett.* **10**, 1529 (2010).
- [129] Arndt, M., Nairz, O., Vos-Andreae, J., Keller, C., van der Zouw, G., and Zeilinger, A. *Nature* **401**, 680 (1999).
- [130] Avouris, P., Chen, Z., and Perebeinos, V. *Nat. Nanotechnol.* **2**, 605 (2007).
- [131] Guisinger, N. P. and Arnold, M. S. *MRS Bulletin* **35**, 273 (2010).
- [132] Largo, A., Redondo, P., and Barrientos, C. *J. Am. Chem. Soc.* **126**, 14611 (2004).
- [133] J. Cernicharo, M. G. and Kahane, C. *Astron. Astrophys. Suppl.* **142**, 181 (2000).
- [134] Fuente, A., Cernicharo, J., Barcia, A., and Gomez-Gonzalez, J. *Astron. Astrophys.* **231**, 151 (1990).

- [135] Rayon, V. M., Redondo, P., Barrientos, C., and Largo, A. *Chem. Eur. J.* **12**, 6963 (2006).
- [136] Yosida, Y. *Physica B* **229**, 301 (1997).
- [137] Ruschewitz, U. *Coord. Chem. Rev.* **244**, 115 (2003).
- [138] Xiao, B., Feng, J., Chen, J. C., and Yu, L. *Chem. Phys. Lett.* **448**, 35 (2007).
- [139] Karen, P., Kjekshus, A., Huang, Q., and Karen, V. L. *J. Alloys Compd.* **282**, 72 (1999).
- [140] Atoji, M. and Medrud, R. C. *J. Chem. Phys.* **31**, 332 (1959).
- [141] Ruiz, E. and Alemany, P. *J. Phys. Chem.* **99**, 3114 (1995).
- [142] Reckeweg, O., Baumann, A., Meyer, H. A., Glaser, J., and Meyer, H. J. *Z. Anorg. Allg. Chem.* **625**, 1686 (1999).
- [143] V. Vohn, W. K. and Ruschewitz, U. *J. Alloys Compd.* **284**, 132 (1999).
- [144] Zaleski-Ejgierd, P., Hakala, M., and Pyykkö, P. *Phys. Rev. B* **76**, 094104 (2007).
- [145] Hume-Rothery, W., Smallman, R., and Haworth, C. *Structure of Metals and Alloys*. Institute of Metals, London, (1969).
- [146] Stowe, A. C., Shaw, W. J., Linehan, J. C., Schmid, B., and Autrey, T. *Phys. Chem. Chem. Phys.* **9**, 1831 (2007).
- [147] Hu, M. G., Geanangel, R. A., and Wendlandt, W. W. *Thermochim. Acta* **23**, 249 (1978).
- [148] Sit, V., Geanangel, R. A., and Wendlandt, W. W. *Thermochim. Acta* **113**, 379 (1987).
- [149] Wolf, G., Baumann, J., Baitalow, F., and Hoffmann, F. P. *Thermochim. Acta* **343**, 19 (2000).
- [150] Baitalow, F., Baumann, J., Wolf, G., Jaenicke-Rüßler, K., and Leitner, G. *Thermochim. Acta* **391**, 159 (2002).
- [151] Xiong, Z., Yong, C. K., Wu, G., Chen, P., Shaw, W., Karkamkar, A., Autrey, T., Jones, M. O., Johnson, S. R., Edwards, P. P., and David, W. I. F. *Nature Mater.* **7**, 138 (2008).
- [152] Lankhorst, M. H. R., Ketelaars, B. W. S. M. M., and Wolters, R. A. M. *Nature Mater.* **4**, 347 (2005).
- [153] Jung, M. C., Lee, Y. M., Kim, H. D., Kim, M. G., Shin, H. J., Kim, K. H., Kim, S. A., Song, S. A., Jeong, H. S., Ko, C. H., and Han, M. *Appl. Phys. Lett.* **91**, 083514 (2007).
- [154] Kim, K., Park, J. C., Chung, J. G., Song, S. A., Jung, M. C., Lee, Y. M., Shin, H. J., Kuh, B., Ha, Y., and Noh, J. S. *Appl. Phys. Lett.* **89**, 243520 (2006).

- [155] Njoroge, W. K., Wöltgens, H. W., and Wuttig, M. *J. Vac. Sci. Technol. A* **20**, 230 (2002).
- [156] Maeda, Y., Andoh, H., Ikuta, I., and Minemura, H. *J. Appl. Phys.* **64**, 1715 (1988).
- [157] Men, L., Jiang, F., and Gan, F. *Mater. Sci. Eng. B* **47**, 18 (1997).
- [158] Kim, E., Lee, J., and Kim, Y. *Phys. Status Solidi RRL* **3**, 103 (2009).
- [159] Matsunaga, T. and Yamada, N. *Phys. Rev. B* **69**, 104111 (2004).
- [160] Nonaka, T., Ohbayashi, G., Toriumi, Y., Mori, Y., and Hashimoto, H. *Thin Solid Films* **370**, 258 (2000).
- [161] Woolley, J. C. *J. Electrochem. Soc.* **113**, 465 (1966).
- [162] Zunger, A., Wei, S. H., Ferreira, L. G., and Bernard, J. E. *Phys. Rev. Lett.* **65**, 353 (1990).
- [163] Jang, M., Park, S., Lim, D., Cho, M., Ko, D., Heo, M., Sohn, H., and Kim, S. *Appl. Phys. Lett.* **96**, 052112 (2010).
- [164] Planté, G. *C. R. Acad. Sci.* **50**, 640 (1860).
- [165] Kurzweil, P. *J. Power Sourc.* **195**, 4424 (2010).
- [166] Payne, D. J., Paolicelli, G., Offi, F., Panaccione, G., Lacovig, P., Beamson, G., Fondacaro, A., Monaco, G., Vanko, G., and Egdell, R. G. *J. El. Spectr. Rel. Phen.* **169**, 26 (2009).
- [167] Phillips, J. C. *Bonds and Bands in Semiconductors*. Academic Press, New York, (1973).
- [168] Desclaux, J. P. and Pyykkö, P. *Chem. Phys. Lett.* **29**, 534 (1974).
- [169] Pyykkö, P. *Adv. Quantum Chem.* **11**, 353 (1978).
- [170] Pyykkö, P. *Chem. Rev.* **88**, 563 (1988).
- [171] Christensen, N. E., Satpathy, S., and Pawlowska, Z. *Phys. Rev. B* **34**, 5977 (1986).
- [172] Liu, A. Y., Garcia, A., Cohen, M. L., Godwal, B. K., and Jeanloz, R. *Phys. Rev. B* **43**, 1795 (1991).
- [173] Verstraete, M. J., Torrent, M., Jollet, F., Zérah, G., and Gonze, X. *Phys. Rev. B* **78**, 045119 (2008).
- [174] Planté, G. *Recherches sur l'Électricité de 1859 à 1879*. Gauthier-Villars, Paris, (1883).
- [175] Duisman, J. A. and Giaque, W. F. *J. Phys. Chem.* **72**, 562 (1968).
- [176] Lide, D. R. *CRC Handbook of Chemistry and Physics 74th Edition*. CRC Press, Boca Raton, (1993).

- [177] Holleman, A. and Wiberg, N. *Lehrbuch der Anorganischen Chemie*, 101. Auflage. Walter de Gruyter, Berlin and New York, (1995).

# Acta Universitatis Upsaliensis

*Digital Comprehensive Summaries of Uppsala Dissertations  
from the Faculty of Science and Technology 772*

Editor: The Dean of the Faculty of Science and Technology

A doctoral dissertation from the Faculty of Science and Technology, Uppsala University, is usually a summary of a number of papers. A few copies of the complete dissertation are kept at major Swedish research libraries, while the summary alone is distributed internationally through the series Digital Comprehensive Summaries of Uppsala Dissertations from the Faculty of Science and Technology. (Prior to January, 2005, the series was published under the title "Comprehensive Summaries of Uppsala Dissertations from the Faculty of Science and Technology".)



ACTA  
UNIVERSITATIS  
UPSALIENSIS  
UPPSALA  
2010

Distribution: [publications.uu.se](http://publications.uu.se)  
urn:nbn:se:uu:diva-131331